

Article

Effects of Multi-Directional Seismic Input on Non-Linear Static Analysis of Existing Reinforced Concrete Structures

Cristina Cantagallo ^{*}, Marco Terrenzi , Enrico Spacone and Guido Camata

Department of Engineering and Geology, University G. d'Annunzio of Chieti-Pescara, Viale Pindaro 42, 65127 Pescara, Italy; marco.terrenzi@unich.it (M.T.); enrico.spacone@unich.it (E.S.); guido.camata@unich.it (G.C.)

* Correspondence: cristina.cantagallo@unich.it

Abstract: Recent studies have shown the importance of including the seismic input directionality in nonlinear analyses for an accurate prediction of the structural demand on frame structures. This paper proposes a new method that includes the multi-directionality of the input seismic forces in Nonlinear Static Analyses (NSAs). Conventionally, the pushover (PO) analyses apply monotonically increasing lateral loads in two directions that typically correspond with the building X and Y directions, that in the case of a rectangular plan are parallel to the building sides. Since in general the direction of the seismic input is a priori unknown, the effects of applying the PO load patterns along varying angles are studied in this paper. Two non-code-conforming reinforced concrete buildings are used as a case study. They have identical structural design but the first one is doubly symmetric while the second one has a significant plan asymmetry due to the translation of the center of mass. PO loads are applied to both structures at angles between 0° and 360° with 15° increments. The results of the NSAs are compared with those of multi-directional NHAs applied at the same angles. The structural demands show that the multi-directional NSAs are more conservative than the conventional NSAs, especially at the corners of the asymmetric-plan building where they can yield significantly higher demands. The base shear capacities in the X and Y directions decrease for intermediate angles due to the interaction between the responses in the X and Y directions that can be captured thanks to the columns' fiber section discretization. On average the results of the multi-directional NSAs are closer to those of the NHAs, even though they are generally lower.

Keywords: reinforced concrete structures; multi-directional seismic input; Nonlinear Static Analysis; Pushover Analysis; Non-Linear Response History Analysis; incident angle



Citation: Cantagallo, C.; Terrenzi, M.; Spacone, E.; Camata, G. Effects of Multi-Directional Seismic Input on Non-Linear Static Analysis of Existing Reinforced Concrete Structures. *Buildings* **2023**, *13*, 1656. <https://doi.org/10.3390/buildings13071656>

Academic Editors: Jianwen Pan and Wusheng Zhao

Received: 29 May 2023
Revised: 19 June 2023
Accepted: 27 June 2023
Published: 28 June 2023



Copyright: © 2023 by the authors. Licensee MDPI, Basel, Switzerland. This article is an open access article distributed under the terms and conditions of the Creative Commons Attribution (CC BY) license (<https://creativecommons.org/licenses/by/4.0/>).

1. Introduction

The direction with which an earthquake hits a building strongly influences its structural response, particularly in the case of irregular structures. However, the epicenter–structure direction of future seismic events is unknown and will not most likely coincide with the structure's main horizontal axes. In general, the seismic design of new buildings or the safety evaluation of existing buildings is carried out considering two horizontal components of seismic action. All seismic codes ([1–4], etc.) require, for a 3D model, a bi-directional horizontal ground motion.

Different procedures have been developed to account for the simultaneous application of the seismic components both in linear and in nonlinear analyses. In Response Spectrum Analysis (RSA), when two horizontal components are combined, their effects are typically multiplied by a factor lower than one since applying the two components fully and simultaneously would be unrealistic (in fact, it is highly unlikely that the two ground motion components reach their maximum simultaneously) and over-conservative. More specifically, Newmark and Rosenblueth [5] propose the Square-Root-of-the-Sum-of-the-Squares (SRSS) combination rule: if r indicates a generic Engineering Demand Parameter (EDP), r^2 is computed as the sum of the contributions of the k ground motion components

r_k^2 . This formulation is based on the principle of superimposition of effects and assumes that each component is a Gaussian stochastic process. Newmark [6] and Rosenblueth and Contreras [7] introduce the Percentage Rule, that evaluates r as the sum of 100% r_k plus a percentage λ of the responses r due to the other components. Newmark [6] and Rosenblueth and Contreras [7] indicate that λ should be 40% and 30%, respectively. More recently, Wilson et al. [8] observe that, unlike the SRSS combination, the Percentage Rules are strictly dependent on the reference system selected for the structure at hand and can underestimate the design forces in given members. Menun and Der Kiureghian [9] introduce the CQC3 directional combination rule for Response Spectrum Analysis (RSA). The CQC3 rule computes r as a function of the seismic orientation angle θ and identifies the angle providing the maximum linear response. The seismic orientation angle θ is typically defined as the angle between the seismic input and the X axis of the structure. The CQC3 rule can be considered the general case of the Percentage and SRSS Rules [10,11]. For further details, Wang et al. [12] provide an extensive state-of-the-art review of the above combination rules.

Cimellaro et al. [13] propose a new combination rule for Nonlinear Static Analyses (NSA). First, they carry out eigenvalue analyses on several highly irregular 3D reinforced concrete (RC) buildings. The 3D models are then loaded with monotonically increasing lateral load patterns proportional to the mode shapes and Φ_{1Y} , with the highest participation factors in the building's horizontal X and Y directions, respectively. More specifically, for each model the applied load pattern is equal to

$$\mathbf{M}(\Phi_{1X} + \gamma \Phi_{1Y}) \quad (1)$$

where $0 < \gamma \leq 1$. This procedure, called Bidirectional Pushover Analysis (BPA) by the authors, is applied using different values of γ ranging from 0.2 to 1.0. They then compute the nonlinear base shear–roof displacement curve and the corresponding displacement demand in the X direction based on the N2 method proposed by Fajfar [14]. The basic idea is that the response in the X direction is affected by the lateral loads applied in the Y direction. Finally, the torsional effects are considered following Fajfar et al. [15]. Floor displacements and floor rotations obtained by the BPAs are compared with the corresponding median results obtained by Nonlinear History Analyses (NHAs) carried out considering bidirectional ground motions. The results of their study suggest a 100% + 60% rule for the BPAs in place of the Eurocode 8 [1] 100% + 30% rule. The 100% + 60% pattern corresponds to applying the seismic force at an angle equal to approximately 30°.

The above discussion points to the issue of the multi-directionality of seismic motion. In the case of irregular structures, the response varies considerably depending on the angle of incidence of the seismic input. Given that the input earthquake direction is generally unknown, the assessment of structural demand should consider multiple angles of incidence of the seismic input. The multi-directionality of the seismic input on 3-dimensional (3D) models has been extensively studied using RSAs, Linear History Analyses (LHAs) and more recently NHAs. For instance, [16–18] use RSAs and LHAs, while [19–31] and many others use NHAs. These studies show that the application of the seismic input along a single reference direction can severely underestimate the seismic demand on irregular structures. On the other hand, few studies analyze the effects of seismic multi-directionality on NSAs.

Cannizzaro et al. [32] study the behavior of a masonry building damaged during the 2009 L'Aquila (Italy) earthquake using 12 NSAs with load patterns applied along incidence angles that vary by 30° increments. Cannizzaro et al. [32] consider only the mass proportional load pattern and a unique participation factor Γ for all directions. Each of the 12 pushover (PO) curves is plotted as a function of the input angle and contributes to the construction of a so-called capacity dominium that provides a 3D representation of all the NSA curves obtained for different incident angles. Similarly, Chácara et al. [33] estimate the seismic vulnerability of unreinforced masonry buildings using multi-directional NSAs and the capacity dominium. Kalkbrenner et al. [34] carry out a series of sequential PO

analyses on the 3D model of a highly irregular masonry building located in Chile using mass proportional horizontal load patterns rotated from 0° to 360° with 45° increments. The seismic demands obtained for the different loading directions are compared with those obtained from NHAs with the longitudinal and transversal components of the 27 February 2010 (Mw 8.8) earthquake recorded at the Santiago Central Station. Kalkbrenner et al. [34] report that the failure mechanisms found with the multi-directional PO analyses are in very good agreement with those from the NHAs and with the damage patterns observed in the structure after the actual earthquake.

Ghayoumian and Emami [35] study the response of three low-to-medium-rise code-conforming torsionally irregular building archetypes with mixed-moment-resistant frames and shear walls. They compare the seismic responses along non-principal directions with those along the principal directions parallel to the reference axes. NSAs are carried out for incident angles $0^\circ \leq \theta \leq 360^\circ$ with 10° increments, using an adaptive PO procedure [36,37] with lateral load distributions that are updated to reflect the changes in the mode shapes as the structure response becomes increasingly nonlinear. The study concludes that the seismic demands may be at their maximum along non-principal directions.

The above studies do not specifically refer to existing RC framed buildings and do not present a systematic validation of NSAs and a comparison with NHAs. This study intends to extend this research to validation through multi-directional NSAs of two different existing RC buildings, designed for gravity loads only and thus not conforming to modern seismic design standards of safety and behavior. Each structure is subjected to mass proportional and triangular load patterns oriented along an incident angle θ that varies between 0° and 360° with 15° increments. The effectiveness of the multi-directional NSAs in the case of the two RC buildings is evaluated, analyzing the advantages and disadvantages with respect to NSAs carried out along the reference structural directions. The results obtained with the NSAs are compared with those of NHAs carried out using 20 pairs of ground motion records, oriented along the same incident angles used for the NSAs. This comparison helps assess whether the multi-directional NSA is capable of accounting for the effects of the multi-directionality of the seismic load. The research addresses three important issues still open in the application of multi-directional pushover analyses: (1) how to calculate the target point for multi-directional NSA; (2) how to evaluate the capacity and demand when the pushover load patterns are applied along incident angles different from the reference structural axes; (3) which load patterns should be used in case of multi-directional pushover analyses. Eurocode 8 specifies that at least two load patterns must be applied, one proportional to the masses and the other proportional to the first mode of the structure in the considered direction. The mass-proportional load pattern is still applicable for multi-directional analyses whereas the first-mode-proportional pattern loses meaning. The paper applies a triangular distribution, proportional to the forces obtained with a linear static analysis, consistent with the Eurocode 8 [1] provisions. The corresponding participation factor is readily computed.

2. Case Study Structures and Structural Models

2.1. Case Study Structures

The seismic input multi-directionality effects on the structural demands are assessed through the study of two RC framed buildings called Structure 1 (Str1) and Structure 2 (Str2), respectively. Str1 has the structural scheme of a typical gravity-load building designed in Italy in the 1970s. It has five storeys, each 3.2 m high, and plan dimensions $28.5 \text{ m} \times 15.5 \text{ m}$ (Figure 1). The load-bearing beams (1–8, 9–16, 17–24 and 25–32), the external beams (1–8, 8–32, 1–25 and 25–32) and the stair beams (4–12 and 5–13) have $30 \times 60 \text{ cm}$ cross sections, while all other beams are flat with a $60 \times 24 \text{ cm}$ cross section. Following the dated practice of building design for gravity loads only, the column sections and reinforcements are progressively reduced along the building height, as indicated in Table A1 of Appendix A. The structural plan is similar to that studied by Bosco et al. [38,39].

However, the load-bearing beams are parallel to the X axis here (whereas they are parallel to the Y direction in the original plan) and the beams' cross sections are modified accordingly.

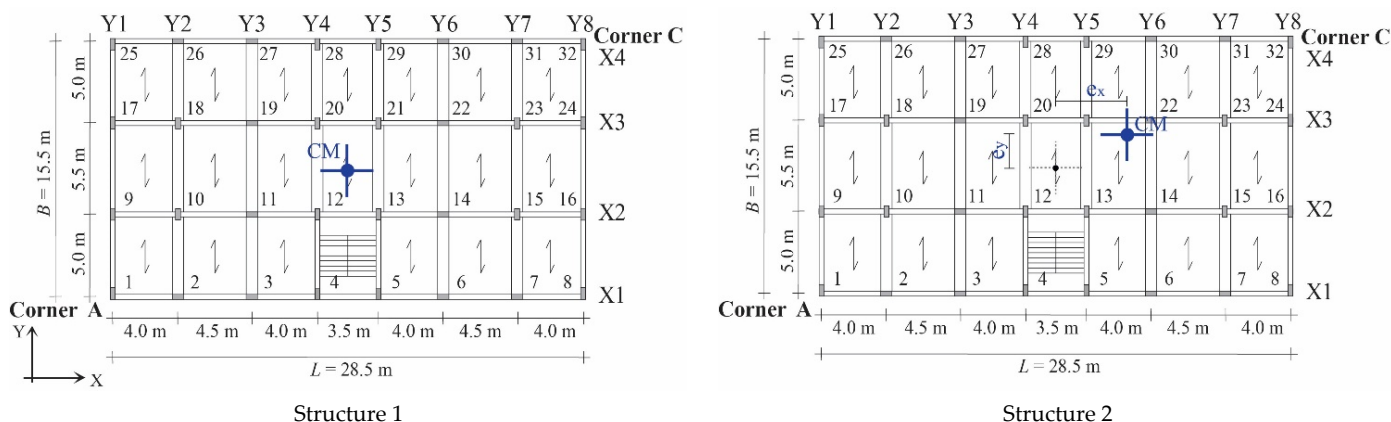


Figure 1. Plan layout of the buildings analyzed in this study.

As indicated in Figure 1, Str2 is identical to Str1, except for the center of mass (CM) that in Str2 has eccentricities equal to $e_x = 15\% L$ and $e_y = 15\% B$ in the X and Y directions, respectively. This eccentricity introduces plan asymmetry because CM does not coincide with the stiffness center. Table A1 in Appendix A gives the cross-section sizes and the reinforcement for each column.

2.2. Structural Models

The two structures are modelled in the computational platform OpenSees [40] using the pre- and post-processor STKO [41]. Their graphical representation is shown in Figure 2. Beams and columns are modelled with *Beam-with-Hinges* elements [42] where the non-linearity is concentrated at the elements' ends, while the behavior of the middle part is linear elastic. To account for cracking in the central linear elastic region the cross-section inertia is reduced to 50% and 75% that of the gross cross section for all beams and columns, respectively. NTC2018 [2] indicates in fact that the stiffness of the cracked elements can be reduced by up to 50% of that of the corresponding uncracked elements. Given that the columns are subjected to compression, the stiffness reduction is lower for the columns. The reduced values are in line with those given by the ACI Building Code [43] for elastic cracked sections. The end hinges' lengths L_{pl} are computed from the following expression used in [1,2,44]

$$L_{pl} = 0.1L_V + 0.17h + 0.24 \frac{d_{bL}f_y(\text{MPa})}{\sqrt{f_c(\text{MPa})}} \tag{2}$$

where h is the section depth, d_{bL} is the (mean) diameter of the tension reinforcement and f_y and f_c are the steel yield stress and the concrete compression strength, respectively. For rectangular columns the plastic hinge length is taken as the average of the values computed with the two section sizes.

The plastic hinge regions are modelled with fiber sections [45], using for steel and concrete the uniaxial constitutive laws Steel01 and Concrete01 [46], respectively. Steel01 is assigned elastic modulus $E_s = 210,000$ MPa, yield strength $f_y = 400$ MPa and strain-hardening ratio $b = 0.005$. Concrete01 has compressive strength $f_c = 28$ MPa, strain at maximum strength $\epsilon_{c0} = 2.5\%$ and ultimate strain $\epsilon_{cu} = 3.5\%$. The fiber section model accounts for the N-M-M interaction [47,48] that becomes important when the columns are subjected to biaxial bending as in the case of the present study.

A floor diaphragm constraint is applied to all floors. Since this constraint generates spurious compressive forces in the beam elements with fiber sections, the axial connection between one of the beam-ends and the structural node it is connected to is released following the approach by Barbagallo et al. [49]. The stairs are not included in the structural models and only their loads are considered. Gravity loads G_k and live loads Q_k

are applied statically before carrying out all nonlinear analyses. The following values are evaluated based on the construction practices and Italian building code of the 1970s [50]: $G_k = 5.6 \text{ kN/m}^2$ and $Q_k = 2.0 \text{ kN/m}^2$ for the slabs, $G_k = 4.2 \text{ kN/m}^2$ and $Q_k = 4.0 \text{ kN/m}^2$ for the stairs and $G_k = 7.0 \text{ kN/m}$ for the infills. The dead loads of each beam and column are automatically added by the program. According to Eurocode 8 [1] and NTC2018 [2], the gravity loads in the seismic load combinations for residential buildings are $G_k + 0.3Q_k$.

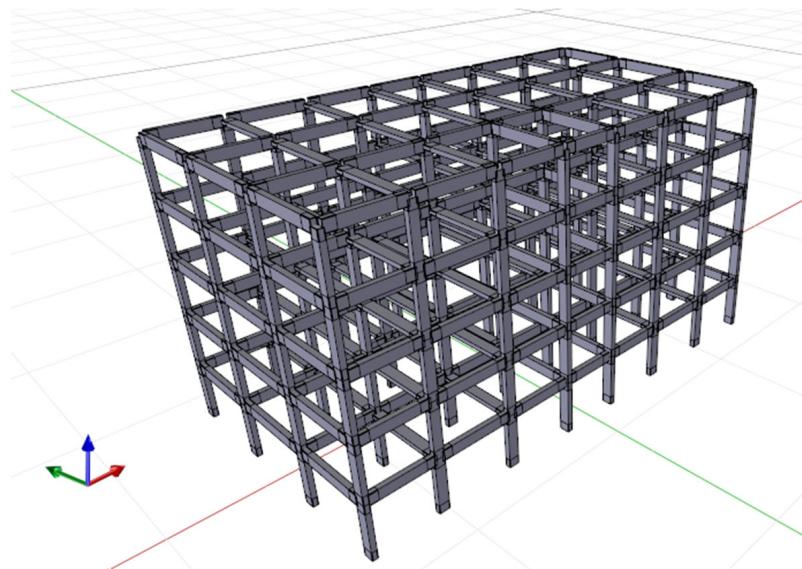


Figure 2. Structural model of the two RC buildings analyzed in this study.

2.3. Modal Analyses

Table 1 shows the results of the modal analyses of the two models after application of the gravity loads. T (s), $M_x(\%)$, $M_y(\%)$ and $R_z(\%)$ are the period of vibration, the x-direction mass participation ratio, the y-direction mass participation ratio and the z-direction rotational mass ratio, respectively. The participating masses show that the first three modes of Str1 are uncoupled, with translational first and third modes while the second mode is torsional. In Str2, despite the high eccentricity of the mass, the first mode remains mostly translational in the X direction as the structure is quite stiff in this direction and quite flexible in the Y direction. Conversely, the second and third modes are strongly coupled. While Str1 is almost doubly symmetric, with a minor mass eccentricity due to the staircase gravity loads, Str2 has a high eccentricity of CM that generates a strong asymmetry of the building.

Table 1. Modal periods (sec) and participation masses (%) of the first three modes of the two structural models after the application of the gravity loads.

Structure 1				Structure 2			
T (s)	$M_x(\%)$	$M_y(\%)$	$R_z(\%)$	T (s)	$M_x(\%)$	$M_y(\%)$	$R_z(\%)$
1.50	0.00	76.19	0.00	1.61	1.0	67.7	8.2
1.07	0.02	0.00	78.78	1.10	41.1	6.7	31.6
0.99	81.44	0.00	0.02	0.89	39.3	39.8	39.0

3. Ground Motion Record Selection

The selection of the ground motions for the NHAs is carried out considering the M_w -R bins providing the largest contribution to the seismic hazard for the probability of exceedance of 10% in 50 years for the reference site located on rock soil at L'Aquila (AQ-Italy)— 42.350° latitude and 13.399° longitude, as indicated in the seismic hazard disaggregation [51] provided by Barani et al. [52]. The analysis of the seismic hazard disaggregation leads to a preselection of

55 pairs of ground motion records (each consisting of two orthogonal horizontal components). These records are selected from two databases, the European Strong-motion Database ESD [53] and the Engineering Strong-Motion database ESM [54] and are characterized by moment magnitude M_w ranging from 5.5 to 7.5, epicentral distance R from 0 to 50 km and soil class A.

Given this earthquake scenario, a set of 20 pairs of ground motion records is selected according to the following spectrum-compatibility criterion [1]: in the $0.2T_1 - 2T_1$ range of periods, no value of the average elastic spectrum should be less than 90% of the corresponding Uniform Hazard Spectrum (UHS). For this study, a 110% upper bound is added to the previous lower bound. Following Beyer and Bommer [55], for each record pair, a single response spectrum $S_a(T_i)$ at given sample periods T_i is computed as the geometric mean of the two corresponding horizontal spectral components S_{aX} and S_{aY} , that is $S_a(T_i) = \sqrt{S_{aX}(T_i) \cdot S_{aY}(T_i)}$. For each ground motion record, the resulting response spectrum is then scaled to the spectral acceleration at T_1 of the UHS and both acceleration components are scaled by the same Scale Factor (SF). Since the first vibration periods of the two structures are similar, a single selection is used with $T_1 = 1.5$ s. Figure 3 compares the response spectra scaled to T_1 (grey lines), the average spectrum (red line), the UHS (black lines), the 90% and the 110% bounds and the spectrum-compatibility range considered for the ground motion selection.

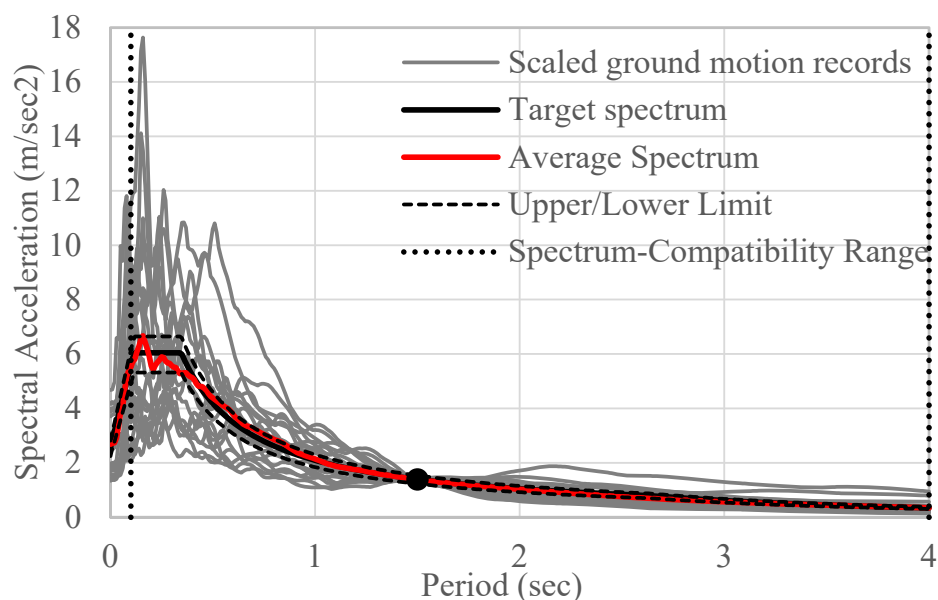


Figure 3. Scaled geometric response spectra, average response spectrum and target UHS of the 20 record pairs selected for $T_R = 475$ yrs.

Table A2 in Appendix B gives the seismological features of the 20 selected ground motion records (Database, Code of the Station, Name, Earthquake Date, Time, Moment Magnitude M_w , Epicentral Distance R , Site Class and Scale Factor).

4. Analysis Results and Discussion

4.1. Multi-Directional Nonlinear Static Analyses

The case study structures are subjected to multi-directional NSAs. Load patterns are applied along incident angles $0^\circ \leq \theta \leq 360^\circ$ that are rotated with increment $\Delta\theta = 15^\circ$ (Figure 4). The conventional loading directions required by the current seismic codes [1,2] for the NSAs coincide with the incident angles $\theta = 0^\circ, 90^\circ, 180^\circ$ and 270° .

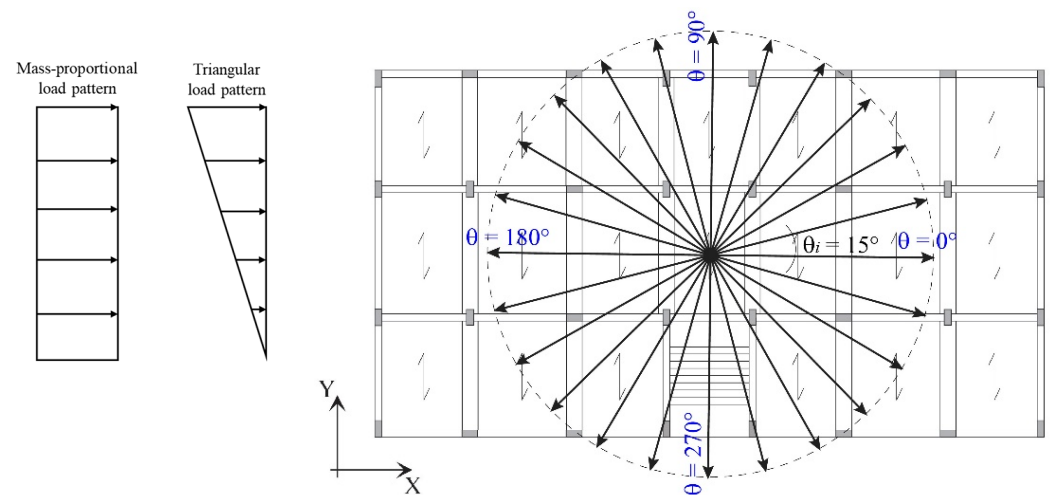


Figure 4. Loading patterns (left) and directions (right) in the multi-directional analyses.

For NSAs, Eurocode 8 [1] recommends the use of the “uniform” and “modal” loading patterns. The first consists of lateral forces proportional to the floor masses (representative of the first mode for a structure with a soft and possibly damaged bottom floor), while the second is proportional to the mass matrix multiplied by the first elastic mode shape in the loading direction (alternatively, a triangular approximation of the first mode shape is often used). The original N2 method was developed for regular buildings and prescribes application of a loading pattern in the building’s “principal” directions. However, it has become common practice to apply the original N2 method to buildings with increasing plan irregularity and/or asymmetry, neglecting the corrections to the method proposed in order to account for the higher mode effects both in plan and in height [15,56]. This work investigates the effects of applying the lateral load in directions different from the reference X and Y axes. In this case, the mass proportional loading still retains its meaning while the modal loading pattern is more difficult to define and justify. For this reason, the two case study structures are analyzed by applying along each θ direction a mass proportional load pattern and a triangular load pattern. Two capacity curves are obtained in the X and Y directions and each of them is transformed into the response of an equivalent single-degree-of-freedom (SDOF) system using the participation factor $\Gamma = \frac{\sum m_i \Phi_i}{\sum m_i \Phi_i^2}$ where m_i is the mass of floor i and Φ_i is the applied load shape. It is worth recalling that in the N2 method derivation [14,57] the loading function is $m_i \Phi_i$, while the response displacement shape is assumed to be proportional to Φ_i . For each incident angle θ , for a mass proportional load $\Gamma = 1$, while for a triangular load vector $\Phi_i \Gamma > 1$. Each SDOF capacity curve is then bi-linearized using an equal energy approach and an ultimate displacement that corresponds to a 20% base shear drop with respect to the peak base shear [2,44]. For each incident angle θ , the structural demands are computed along the X and Y structural directions according to the original N2 method [14], superimposing the elastic spectrum (with 5% damping) of the considered site on the bi-linearized capacity curve. The application of the N2 method leads to different structural demands for each reference direction X and Y and for each incident angle θ .

Figures 5 and 6 show the capacity curves obtained from mass proportional and triangular load patterns applied to Str1 and Str2, respectively. The first and second rows refer to mass proportional and triangular load patterns, respectively, while the first and second columns refer to the X and Y directions, respectively. Each Figure shows the base shear vs top floor CM displacement for $0^\circ \leq \theta \leq 360^\circ$. The solid black curves refer to $\theta = 0^\circ, 90^\circ, 180^\circ$ and 270° (i.e., the classical loading directions), while the colored curves indicate the responses for intermediate values of θ . In general, the variability of these curves shows how much the structural capacity depends on the incident angle. More specifically, the biaxial effects are evident as the capacity curves for $\theta \neq 0^\circ, 90^\circ, 180^\circ$ and

270° have lower capacities than those for POs in the principal structural directions. These effects are captured because the fiber sections account for the biaxial bending nonlinear interaction. The curves for Str2 show a higher variability than those of Str1, because of its higher plan irregularity. For both structures, loading patterns and structural directions, the capacity curves for $\theta = 0^\circ, 90^\circ, 180^\circ$ and 270° envelope the curves obtained for the other loading directions.

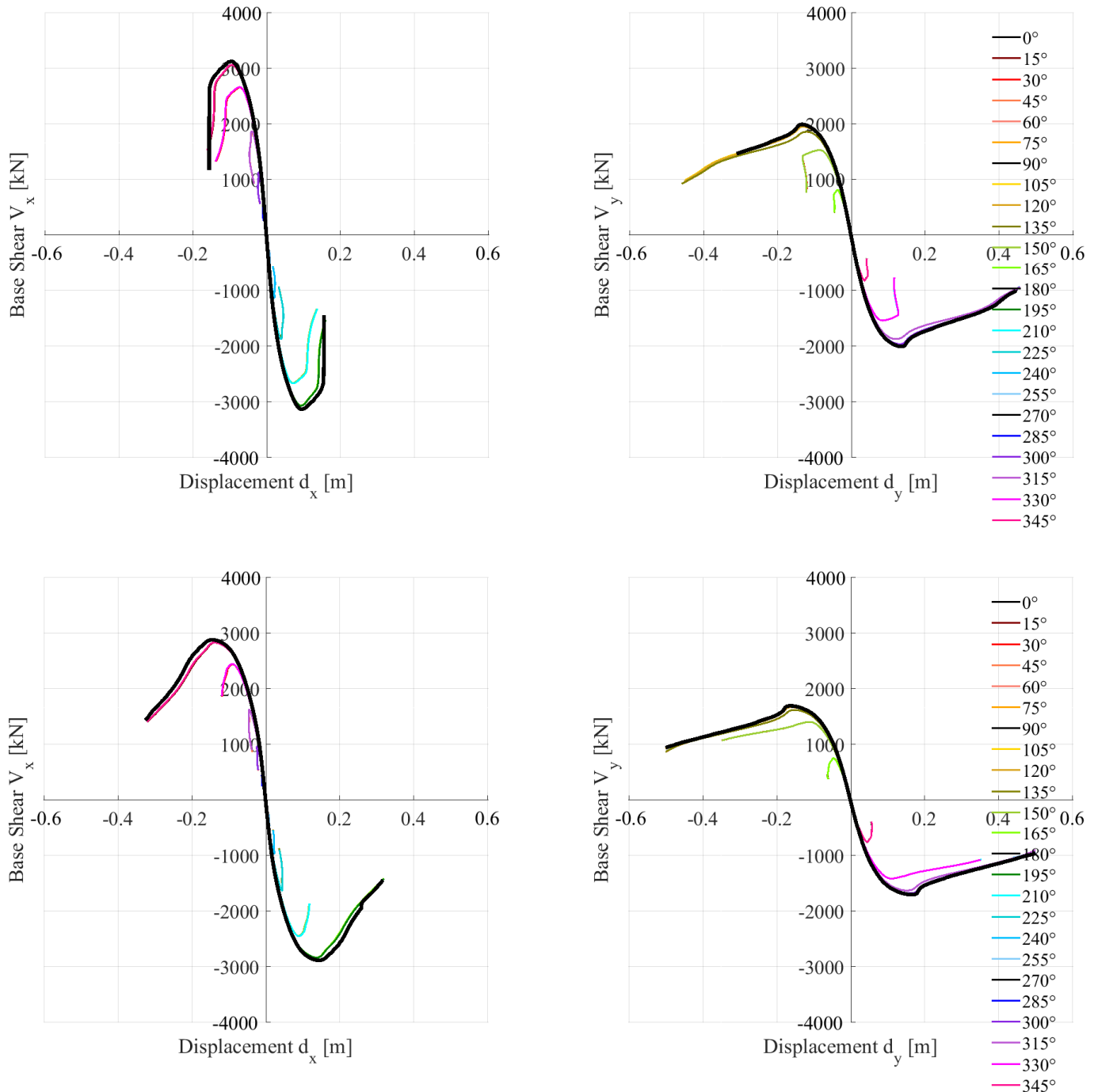


Figure 5. Structure 1 capacity curves in the X (left) and Y (right) directions for mass proportional (top) and triangular (bottom) load patterns applied at incident angles $0^\circ \leq \theta \leq 360^\circ$.

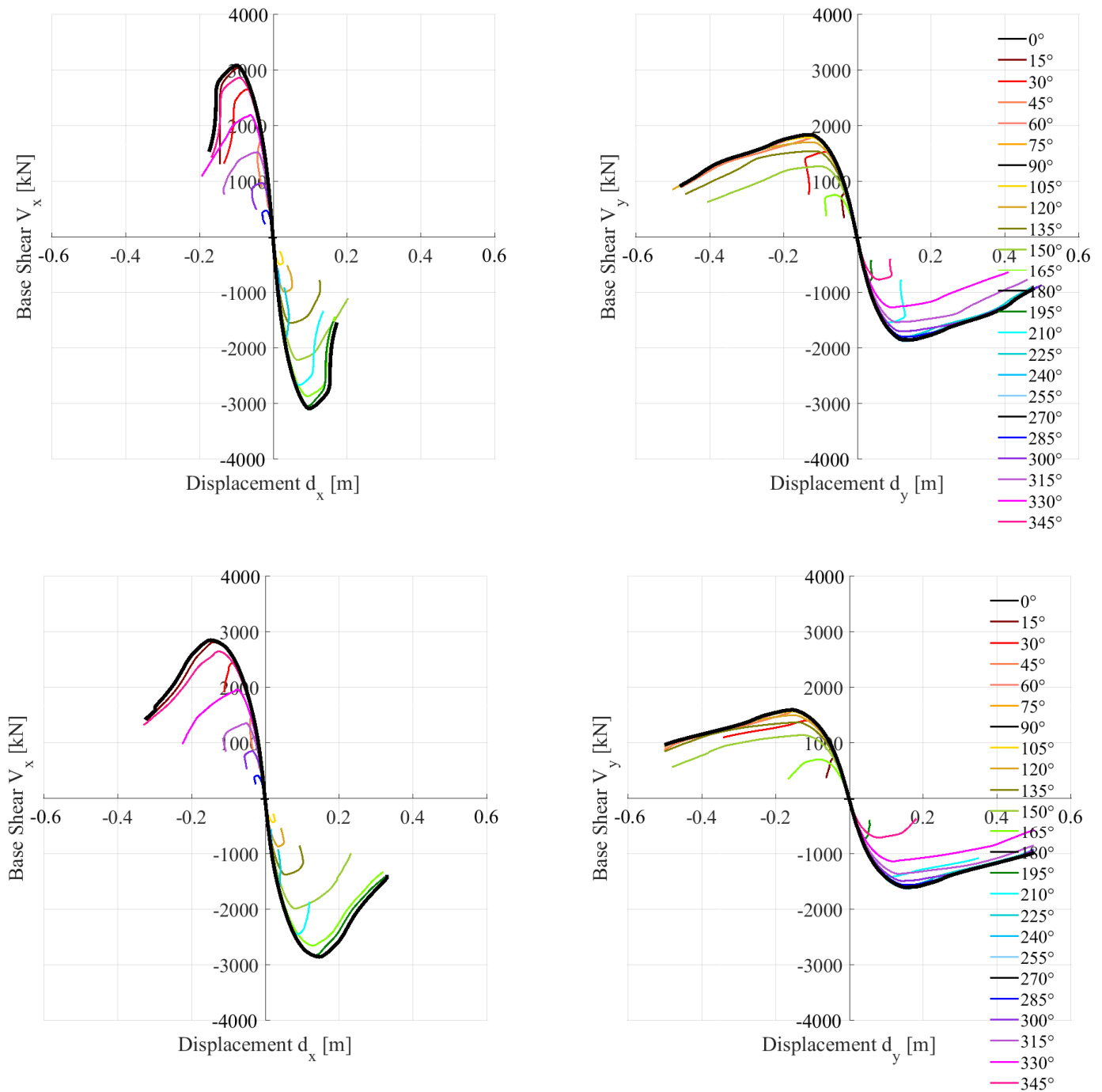


Figure 6. Structure 2 capacity curves in the X (left) and Y (right) directions for mass proportional (top) and triangular (bottom) load patterns applied at incident angles $0^\circ \leq \theta \leq 360^\circ$.

In order to investigate the structural behavior in the X and Y directions when the load pattern is applied along θ , as an example Figure 7 shows the capacity curves of Str1 in the X (left) and Y (right) directions for a mass proportional load pattern applied at incident angles $\theta = 15^\circ, 30^\circ$ and 45° . The figure shows that, at $\theta = 15^\circ$, when the base shear reaches its maximum value in the X direction, in the Y direction the curve is almost elastic and subsequently its descending branch begins for V_y values much smaller than the maximum base shear in the Y-direction for $\theta = 0^\circ$. Similarly, for $\theta = 30^\circ$, V_x and V_y reach simultaneously their maximum values but while d_x increases d_y decreases. For $\theta = 45^\circ$, V_x and V_y have similar maximum values, but the V_x curve quickly drops and unloads, while V_y shows a rather ductile response. Similar conclusions can be drawn for Str2.

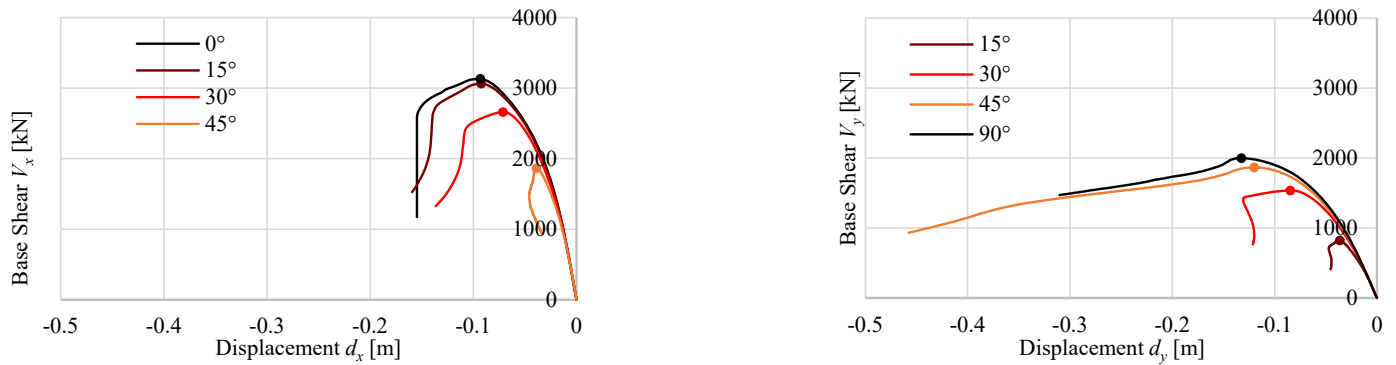


Figure 7. Structure 1 capacity curves in the X (left) and Y (right) directions for mass proportional load pattern applied at incident angles $\theta = 0^\circ, 15^\circ, 30^\circ, 45^\circ$ and 90° .

When the structure is pushed along a θ direction, the structure moves along a direction that is in general different from θ and can change continuously. Figures 8 and 9, for example, show the displacement paths followed by Str1 under mass proportional and triangular load patterns, respectively. More specifically, each figure shows five plots, for load paths along $\theta = 0^\circ, 15^\circ, 30^\circ, 45^\circ, 60^\circ$ and 75° , respectively. When $\theta > 30^\circ$ the response becomes increasingly nonlinear, and the structure moves along its weak Y direction. This behavior is due to the large difference in stiffness and strength in the X and Y directions. Very similar patterns are found for Str2.

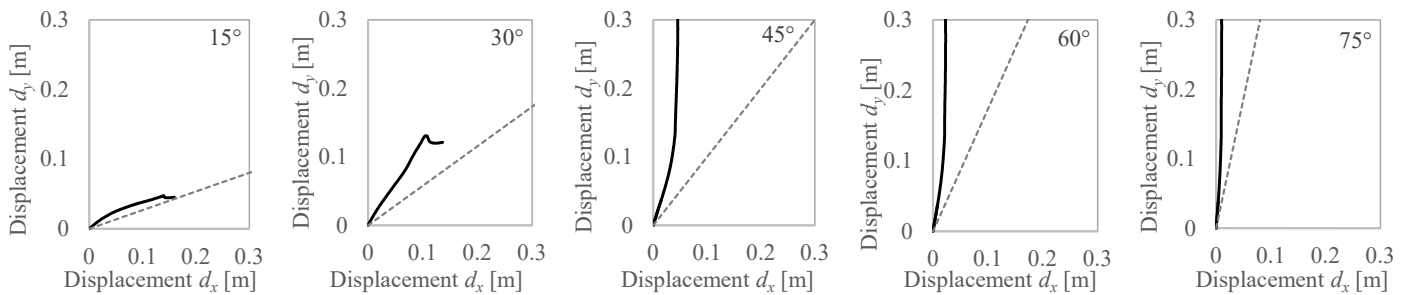


Figure 8. Displacements of Structure 1 for a mass proportional load pattern along $0^\circ < \theta < 90^\circ$. The dotted line indicates the loading direction while the full line indicates the displacement points.

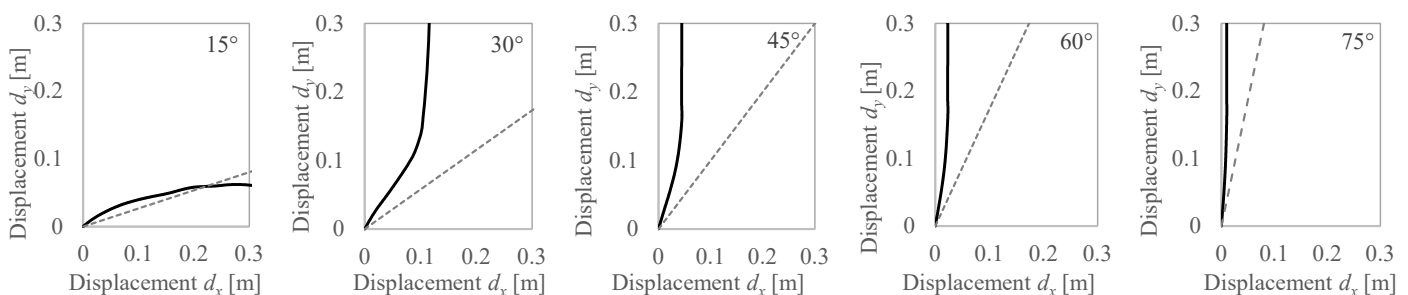


Figure 9. Displacements of Structure 1 for a triangular load pattern along $0^\circ < \theta < 90^\circ$.

To visualize the structures' capacity variation for different incident angles θ , Figures 10 and 11 show in red the peak base shear $V_{b,max,\theta}$ in the loading direction θ normalized with respect to $V_{b,max,0}$, that is the maximum V_b for $\theta = 0^\circ$. The same figures show in blue the maximum displacements $d(V_{b,max,\theta})$ corresponding to $V_{b,max,\theta}$, normalized with respect to $d(V_{b,max,0})$. As previously discussed, the maximum displacement is not parallel to θ . It is computed as $\sqrt{d_x^2 + d_y^2}$ corresponding to $V_{b,max,\theta}$. Figure 10 refers to Str1, while Figure 11 refers to Str2. In both figures, the left plot refers to mass proportional and

the right to triangular loads. Figure 10 shows that for Structure 1 the capacity in terms of base shear ($V_{b,max,\theta}$) is maximum at 0° and minimum at 90° . Conversely, the displacement $d(V_{b,max,\theta})$ is maximum at 90° and minimum at 0° . This behavior is coherent with the structural configuration, characterized by deep beams and columns oriented along 0° . Figure 11 shows that the structural behavior of Structure 2 is not symmetric. The minimum capacity $V_{b,max,\theta}$ occurs in fact at $\theta = 90^\circ, 105^\circ$ and $\theta = 270^\circ, 285^\circ$.

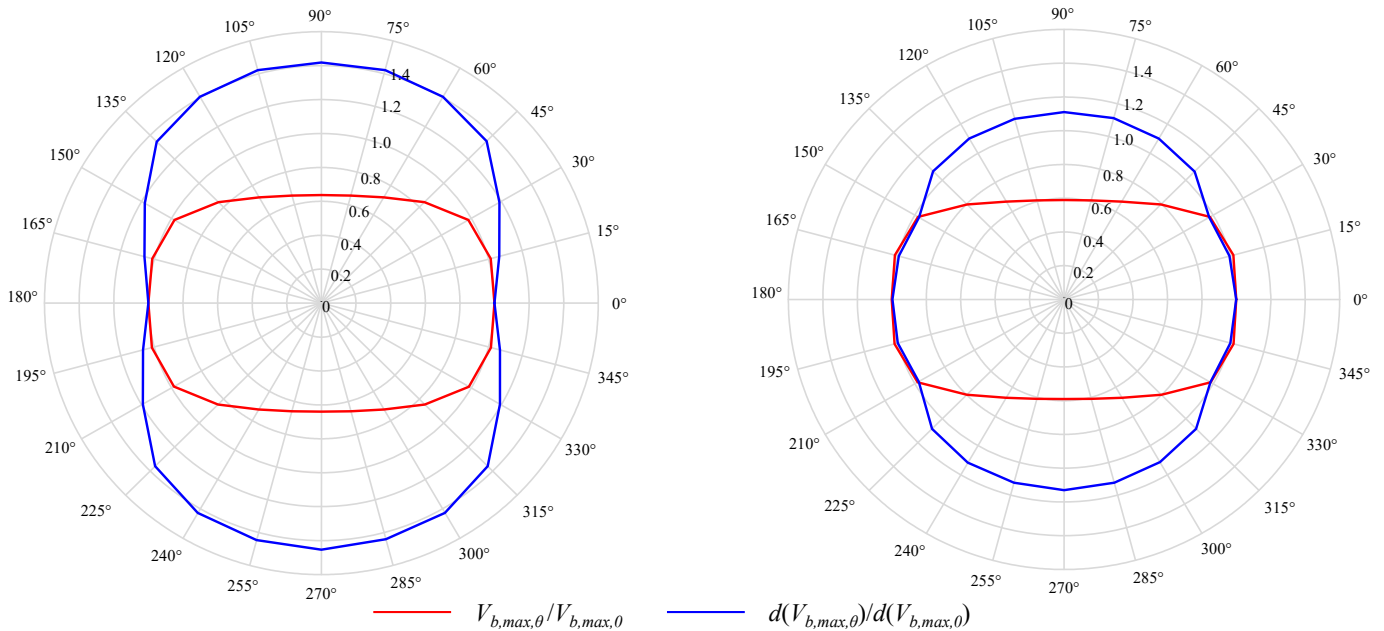


Figure 10. Structure 1. $V_{b,max,\theta}/V_{b,max,0}$ (red) and $d(V_{b,max,\theta})/d(V_{b,max,0})$ (blue) ratios for mass proportional (left) and triangular (right) load patterns.

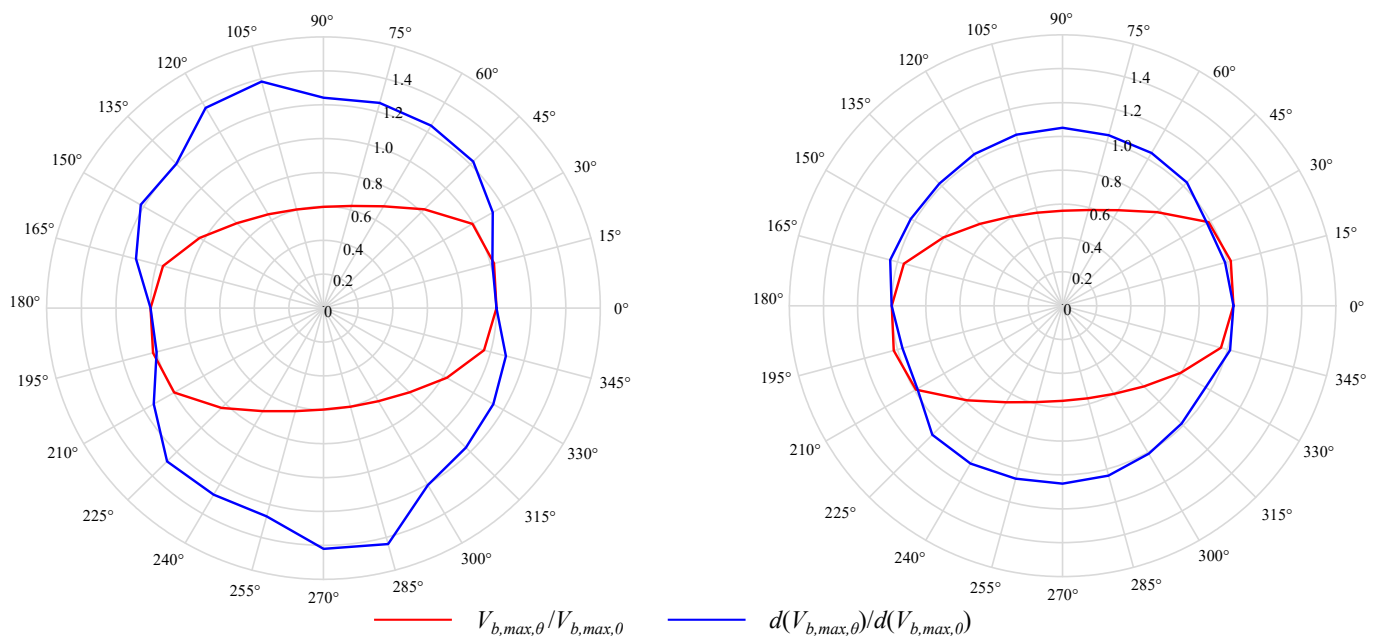


Figure 11. Structure 2. $V_{b,max,\theta}/V_{b,max,0}$ (red) and $d(V_{b,max,\theta})/d(V_{b,max,0})$ (blue) ratios for mass proportional (left) and triangular (right) load patterns.

Figures 12 and 13 show in red the peak base shear $V_{b,max,XY}$ for loading at an angle θ normalized with respect to $V_{b,max,0}$. $V_{b,max,XY}$ is defined looking at Figure 7: for a given angle θ , $V_{b,max,XY}$ is either $V_{b,max,X}$ or $V_{b,max,Y}$ and refers to the curve that reaches the peak and then

softens (displacement increases) as opposed to the other curve that unloads after the peak (displacement does not change or decreases). It basically represents the base shear capacity in the reference direction that reaches failure and then softens. For example, for the curves of Figure 7, for $\theta = 15^\circ$ and 30° $V_{b,max,XY} = V_{b,max,X}$, while for $\theta = 45^\circ$ $V_{b,max,XY} = V_{b,max,Y}$. In the Y direction ($\theta = 90^\circ$) $V_{b,max,XY}/V_{b,max,0}$ is about 0.6, indicating that the peak base shear in the Y direction is about 60% that of the X direction for both loading patterns. The blue lines show the displacement at $V_{b,max,XY}$ in the same (X or Y) direction $d(V_{b,max,XY})$, normalized with respect to the displacement for $\theta = 0^\circ$ $d(V_{b,max,0})$. The red and blue curves are interrupted when $V_{b,max,XY}$ switches from $V_{b,max,X}$ to $V_{b,max,Y}$ or vice versa.

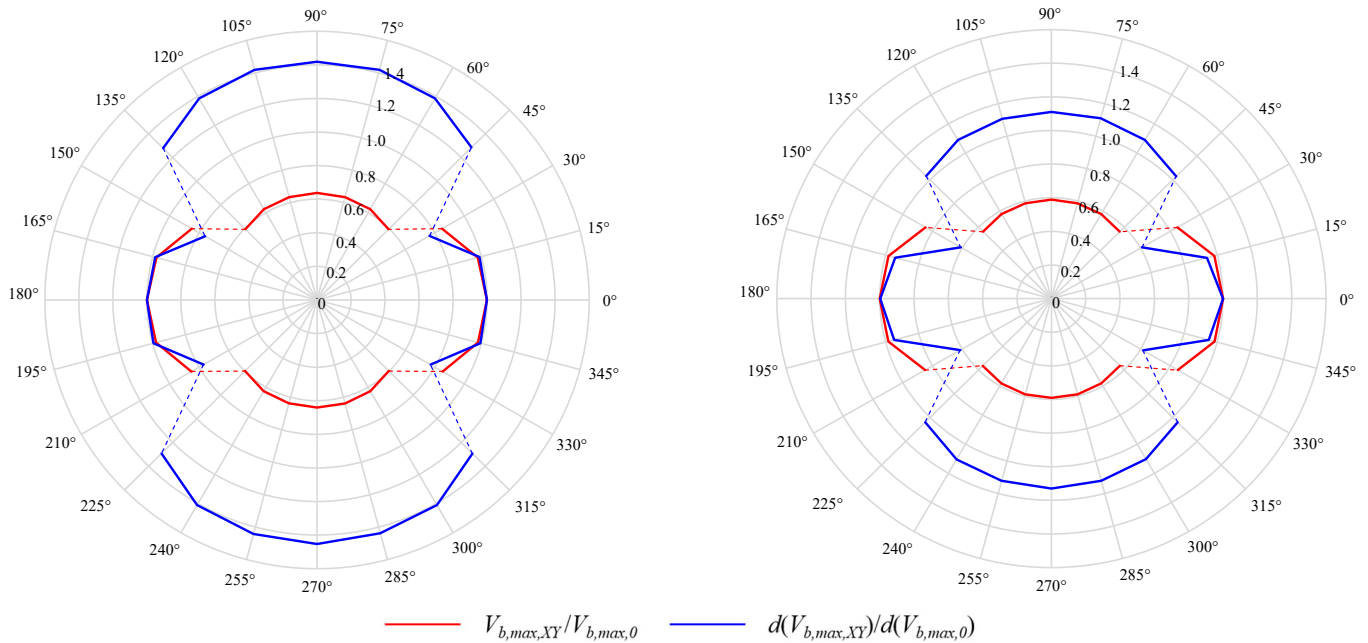


Figure 12. Structure 1. $V_{b,max,XY}/V_{b,max,0}$ (red) and $d(V_{b,max,XY})/d(V_{b,max,0})$ (blue) ratios for mass proportional (left) and triangular (right) load patterns.

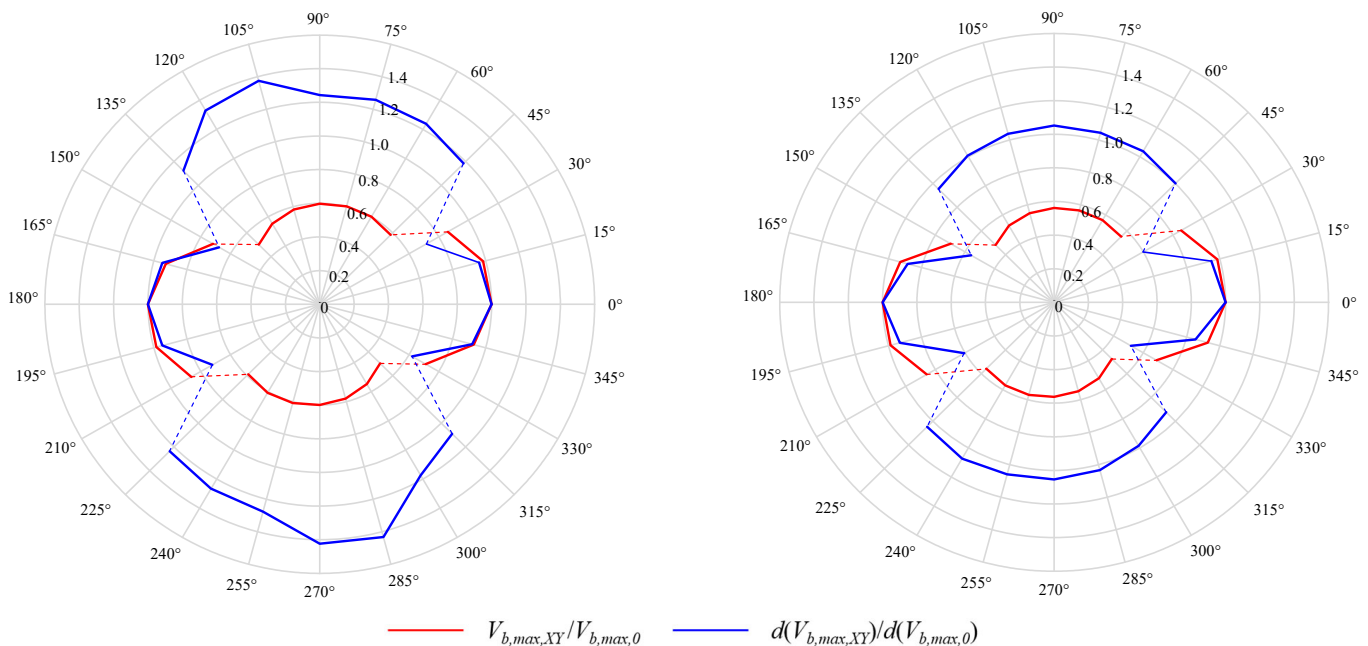


Figure 13. Structure 2. $V_{b,max,XY}/V_{b,max,0}$ (red) and $d(V_{b,max,XY})/d(V_{b,max,0})$ (blue) ratios for mass proportional (left) and triangular (right) load patterns.

Figures 12 and 13 show the ratios $V_{b,max,XY}/V_{b,max,0^\circ}$ and $d(V_{b,max,XY})/d(V_{b,max,0^\circ})$ for mass proportional (left) and triangular (right) load patterns on Str1 and Str2, respectively. The two figures show that the ratios $d(V_{b,max,XY})/d(V_{b,max,0^\circ})$, are greater than one at $\theta = \pm 90^\circ \pm 180^\circ$, especially for the mass proportional load pattern, and lower than one at $\theta = \pm 30^\circ \pm 180^\circ$. This result indicates that the most and least flexible directions of the two structures are $\theta = \pm 90^\circ \pm 180^\circ$ and $\theta = \pm 30^\circ \pm 180^\circ$, respectively. Conversely, the ratios $V_{b,max,XY}/V_{b,max,0^\circ}$ indicate that the weakest directions are $\theta = 30^\circ$ and $\theta = 45^\circ$. For $\theta = 30^\circ$, failure takes place in the X direction with a peak base shear lower (15–20%) than for $\theta = 0^\circ$. For $\theta = 45^\circ$, failure takes place in the y direction with a peak base shear lower (10–15%) than for $\theta = 90^\circ$. The results are similar for mass and for triangular load patterns.

The demand in terms of Interstory Drift Ratio (IDR), that represents the demand on a single story, is considered next. As stated above, the results refer to the pushover in the direction (X or Y) that reaches a peak base shear and then softens with increasing displacements. When both displacements in X and Y increase, the curve with the maximum displacement is selected assuming that the structure reaches its limit state for ductile mechanisms with higher displacements. The structural demand for each θ angle is computed according to the N2 method [14] superimposing the given capacity curve (in the X or in the Y direction) with the target spectrum with $T_R = 475$ years, soil category A and coordinates 42.350° lat. 13.399° long. to find the target displacement. The IDRs are reported at the target displacement.

Figures 14 and 15 show the IDRs in the X and Y directions, respectively, for the multi-directional NSAs on Str1. For both Str1 and Str2, for $0^\circ \leq \theta \leq 30^\circ$, $150^\circ \leq \theta \leq 210^\circ$ and $330^\circ \leq \theta < 0^\circ$ the IDRs are in the X direction, for the other θ angles in the Y direction. Each figure shows the IDRs at CM (left), at Corner A (center) and at Corner C (right) with mass proportional (first row) and triangular (second row) load patterns. The above Corners are indicated in Figure 1. The black lines refer to the NSAs for $\theta = 0^\circ, 90^\circ, 180^\circ$ and 270° . The red lines represent the demand envelopes for all incident angles with the indication of the angle with the highest demand. Figures 16 and 17 show the same results for Str2.

For Str1, the IDRs indicate that at the ground floor the application of a multi-directional NSA leads to a higher demand compared to a conventional NSA along the X and Y directions. At the higher levels, however, the demand of a multi-directional NSA is very close to that of a conventional NSA. The reason for this behavior lies in the almost perfect double symmetry of Str1.

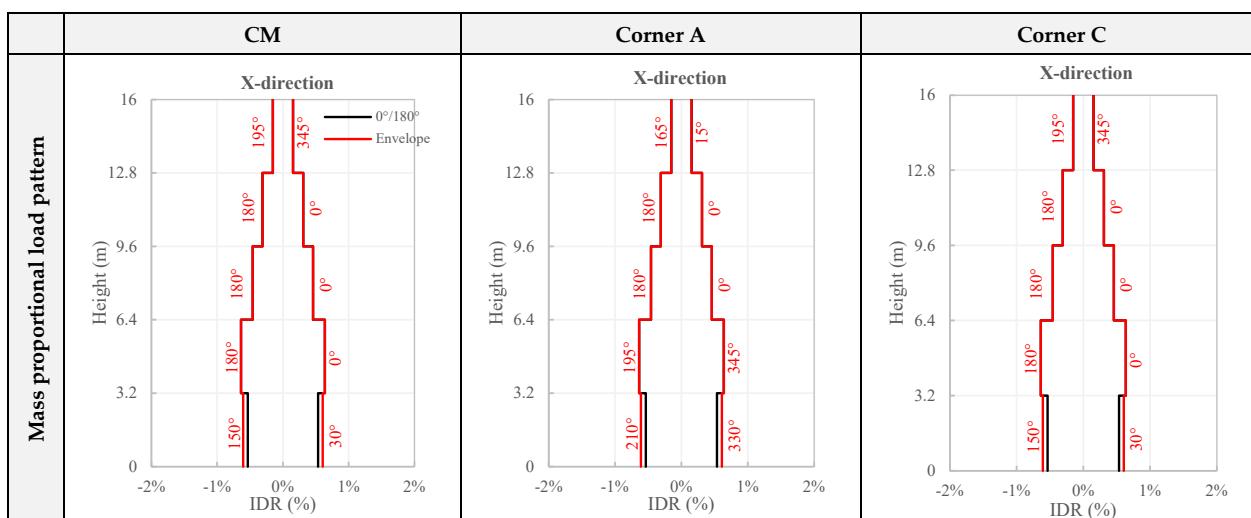


Figure 14. Cont.

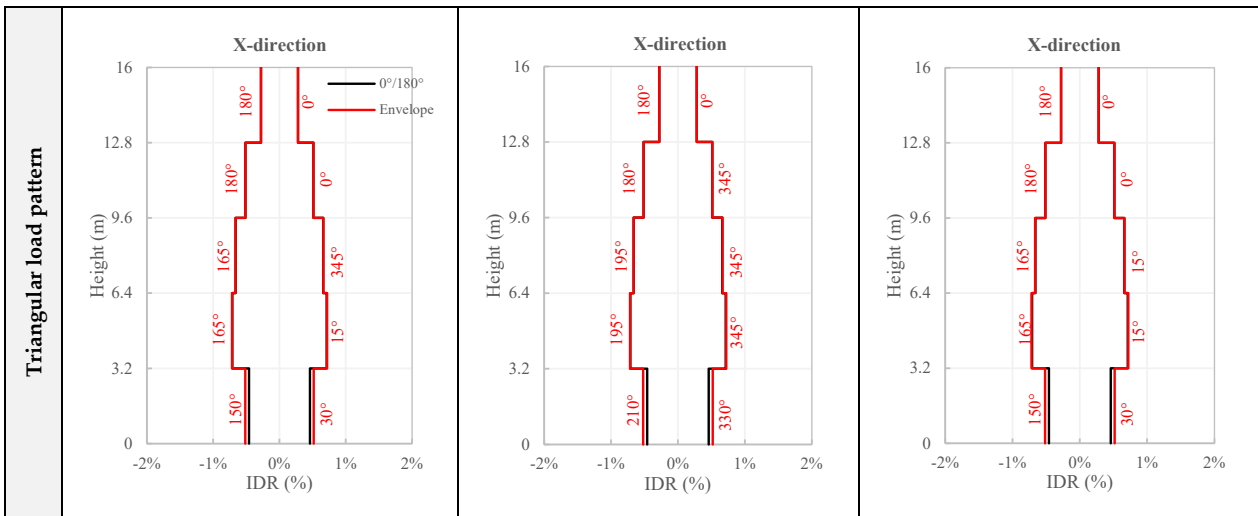


Figure 14. Structure 1 IDRs in the X direction at CM (left), Corner A (center) and Corner C (right) for mass proportional (top) and triangular (bottom) load patterns at incident angles $0^\circ \leq \theta \leq 360^\circ$ with $\Delta\theta = 15^\circ$ increments. The black lines indicate the IDRs corresponding to $0^\circ, 90^\circ, 180^\circ$ and 270° , the red lines indicate the envelope of the multi-directional NSAs and the corresponding maximum demand angle.

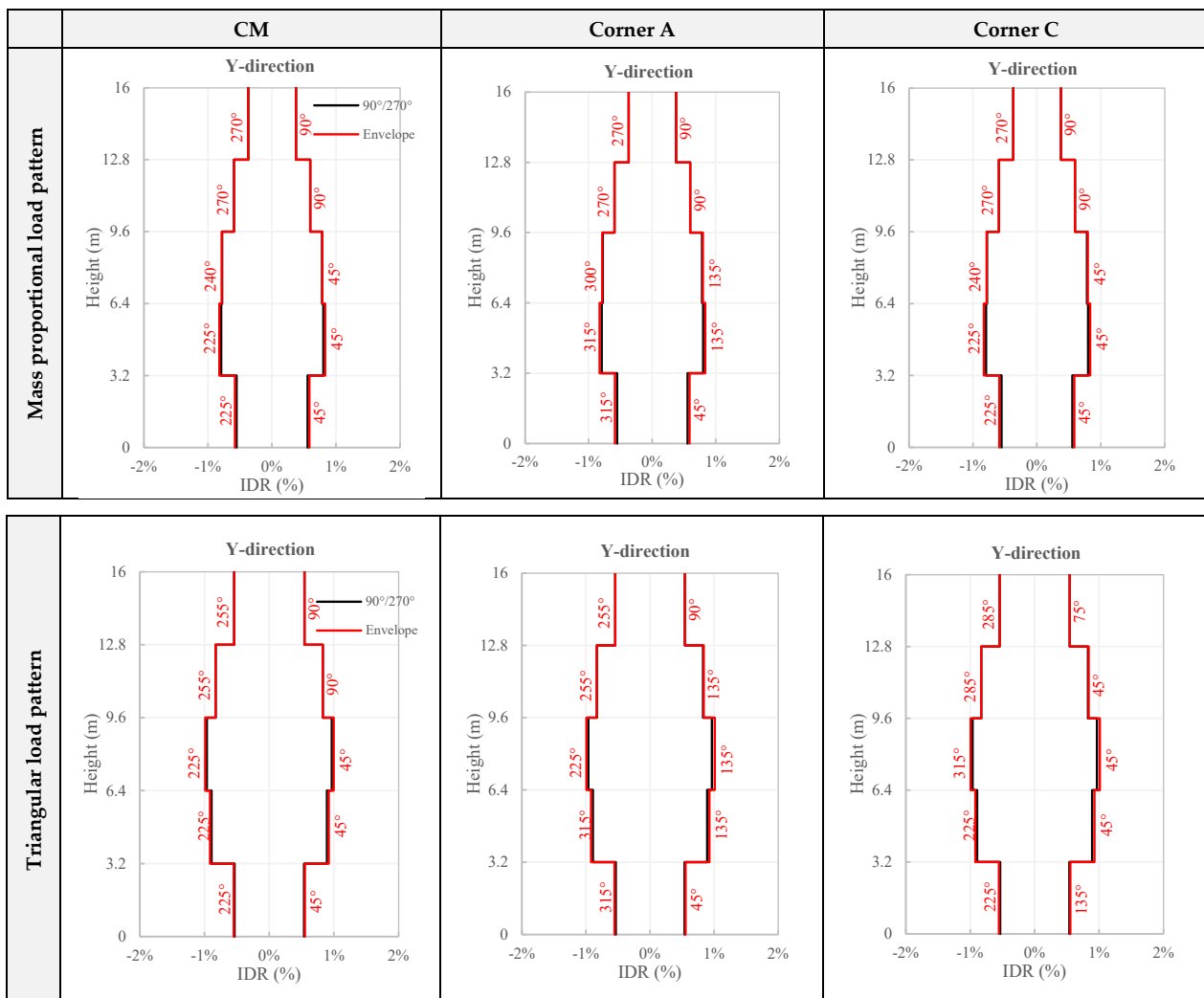


Figure 15. Structure 1 IDRs in the Y direction.

The multi-directional NSAs applied to Str2 (Figures 16 and 17) yield seismic demands significantly higher than those of the conventional NSA, especially at Corners A and C. The most significant case is that of the IDRs in the Y direction at Corner C for the triangular load pattern, where the ground floor demand predicted by the multi-directional NSAs is about 30% higher than that predicted by the NSA along the Y direction. This is mostly due to the asymmetry of Str2.

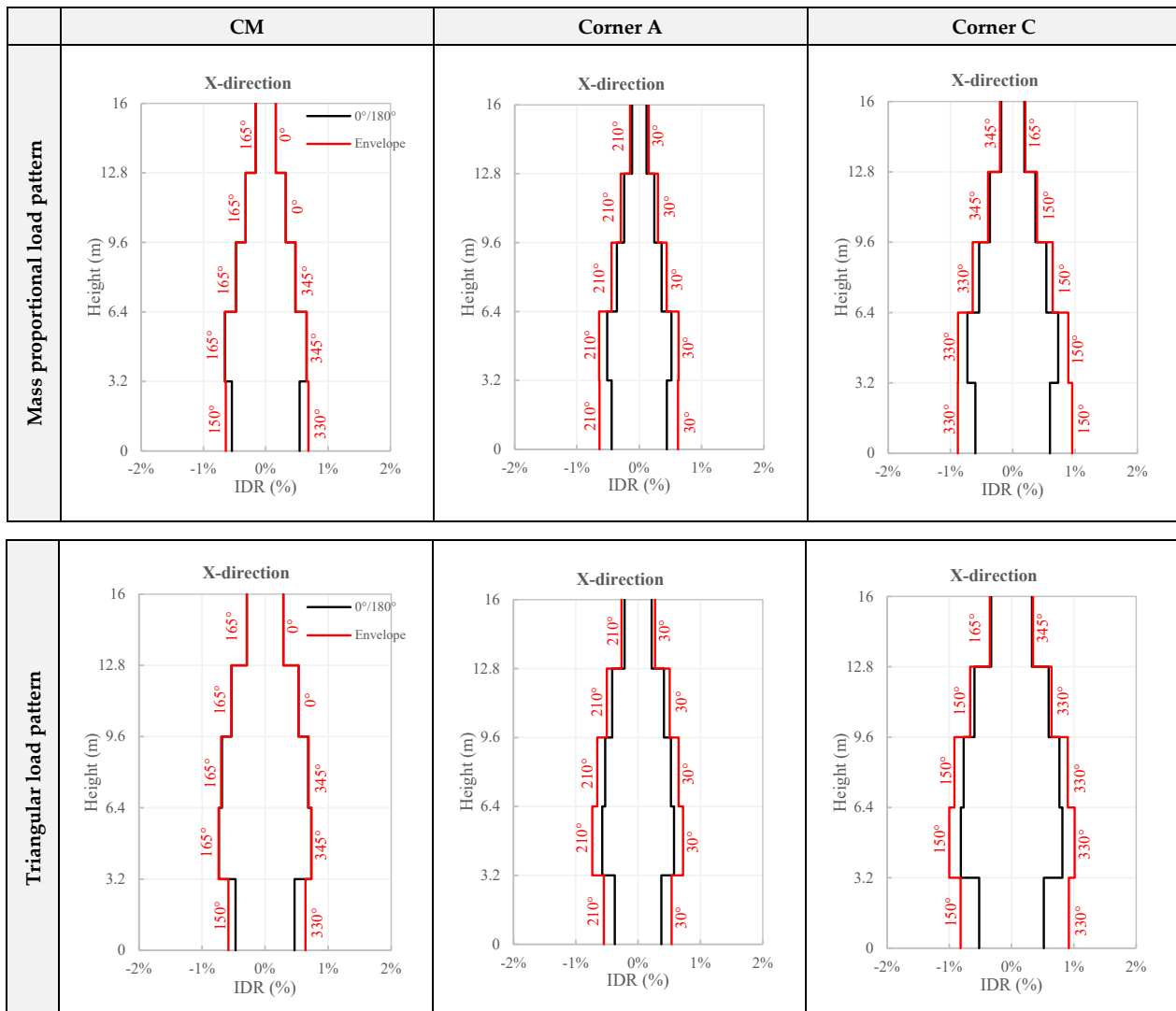


Figure 16. Structure 2 IDRs in the X direction.

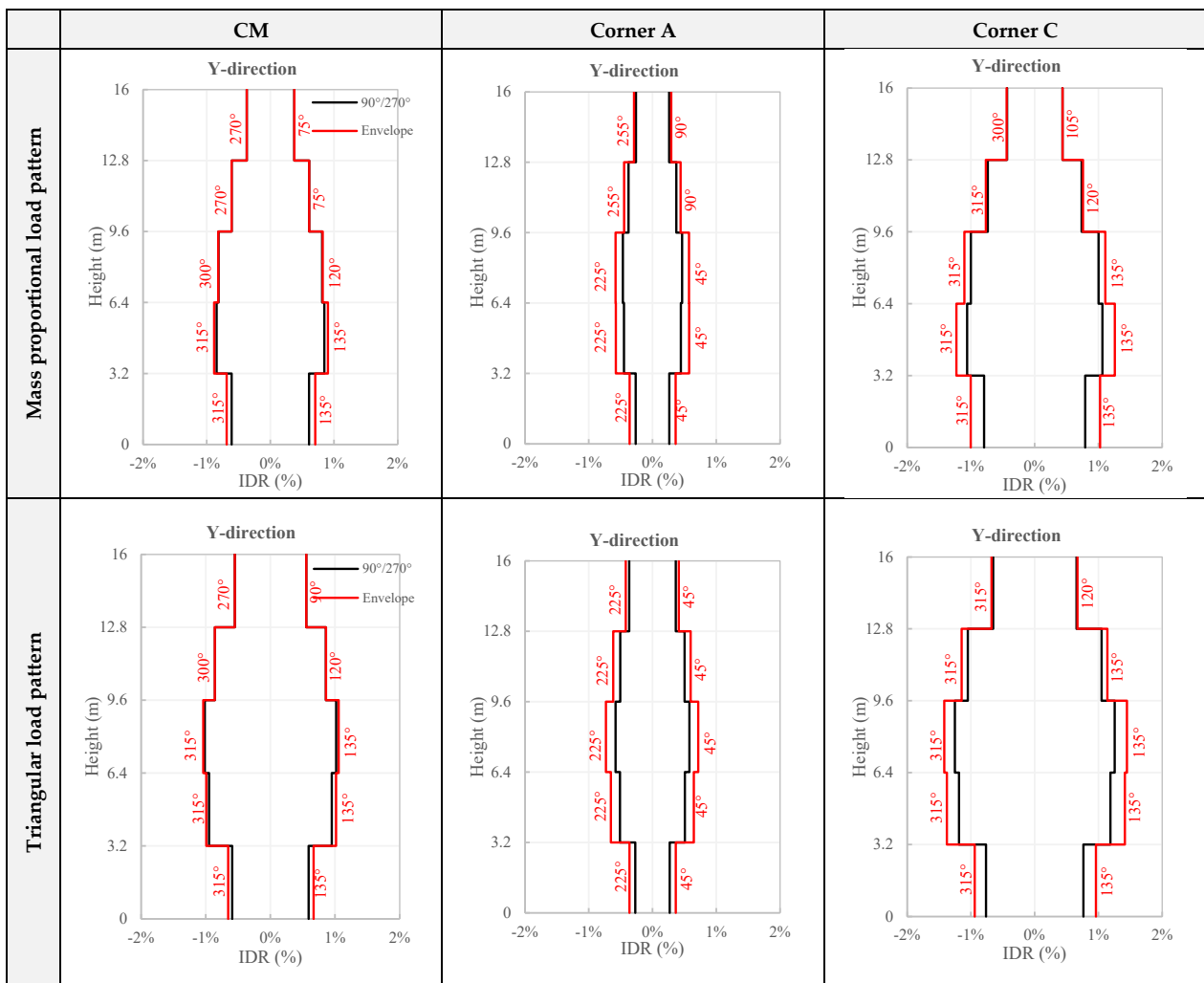


Figure 17. Structure 2 IDRs in the Y direction.

To better quantify the amplification of the seismic demand due to the application of the seismic load along θ on Str2, Figures 18 and 19 show the ratios between the IDRs generated by multi-directional and conventional NSAs. For each θ , IDR_{XY} is the IDR in the loading direction (IDR_X or IDR_Y) where the peak base shear is reached followed by softening. IDR_{XY} is normalized with respect to the IDR obtained for NSA in the corresponding (X or Y) directions. More precisely, the IDRs for $330^\circ \leq \theta \leq 30^\circ$, $150^\circ \leq \theta \leq 210^\circ$, $45^\circ \leq \theta \leq 135^\circ$ and $225^\circ \leq \theta \leq 315^\circ$ are normalized with respect to the IDRs for $\theta = 0^\circ$, $\theta = 180^\circ$, $\theta = 90^\circ$ and $\theta = 270^\circ$, respectively. The results in Figures 18 and 19 refer to mass proportional and triangular load patterns, respectively. Each figure includes three plots, with the results for each structural level, at CM (top), Corner A (center) and Corner C (bottom), respectively. For mass proportional load patterns (Figure 18), the highest IDR_{XY}/IDR ratios are 1.44 and 1.59 and occur for $\theta = 210^\circ$ at Corner A and for $\theta = 330^\circ$ at Corner C, respectively. For triangular load patterns (Figure 19), significant amplifications occur for $\theta = 210^\circ$ at Corner A (1.47) and for $\theta = 330^\circ$ at Corner C (1.77).

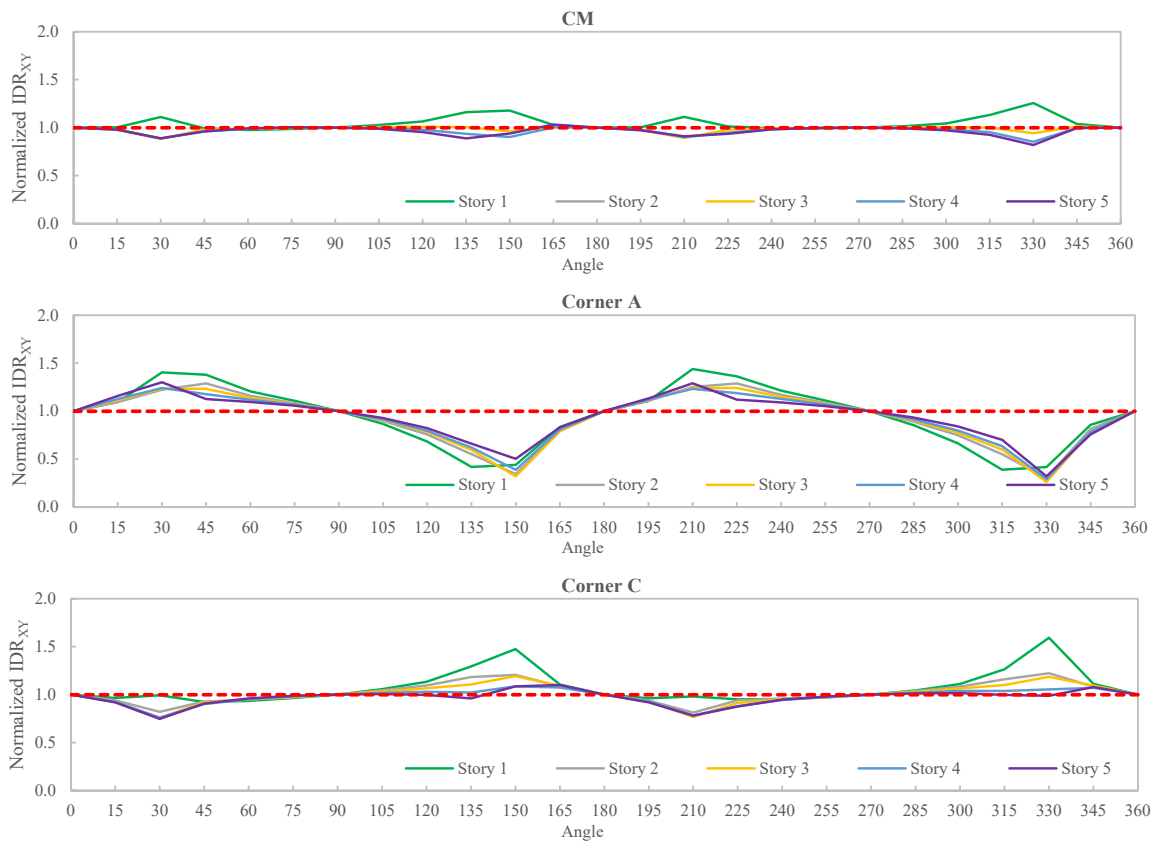


Figure 18. Structure 2. Normalized IDR_{XY} at CM (top), Corner A (center) and Corner C (bottom) for mass proportional load pattern.

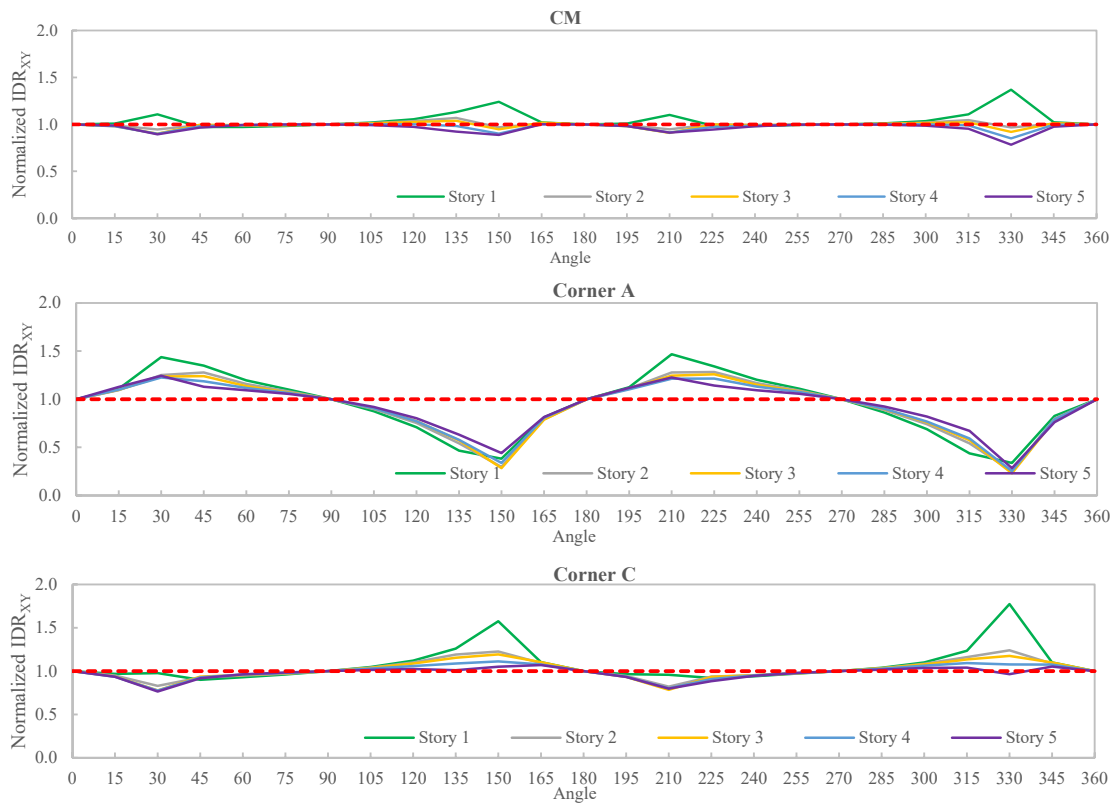


Figure 19. Structure 2. Normalized IDR_{XY} for triangular load pattern.

4.2. Comparison between Multi-Directional Non-Linear Static and Non-Linear History Analyses

The IDRs of the multi-directional NSAs are compared here with the IDRs of the multi-directional NHAs. As indicated in Section 3, the NHAs were carried out using a set of 20 pairs of recorded ground motion records on Str1 and Str2. The structural models use 2% Rayleigh damping (at the first and third mode frequency) with full initial stiffness.

For each of the 20 ground motion pairs, the EW component of the ground motion is oriented along the same 24 θ angles used for the multi-directional NSAs. A total of 480 bidirectional NHAs were carried out for each structure.

For each NHA the maximum $|IDR|$ in the X and Y directions $maxIDR$ over the time history are computed. For each angle θ , the average value of the 20 $maxIDRs$ is found according to the current regulatory codes [1,2], also if other efficient approaches are used in literature [58]. Finally, the envelopes of the average values obtained for each incident angle are plotted. Figures 20–22 show the envelopes of the multi-directional NSAs (red and blue lines for mass proportional and triangular load patterns, respectively) and of the NHAs (black lines) for Str1 at CM, Corner A and Corner C, respectively. Each figure shows the IDRs in the X and Y directions (left and right, respectively). The solid lines refer to the multi-directional NSAs and NHAs, while the corresponding dotted lines refer to the conventional nonlinear analysis (corresponding to $\theta = 0^\circ, 90^\circ, 180^\circ$ and 270°). Similarly, Figures 23–25 show the same results for Str2.

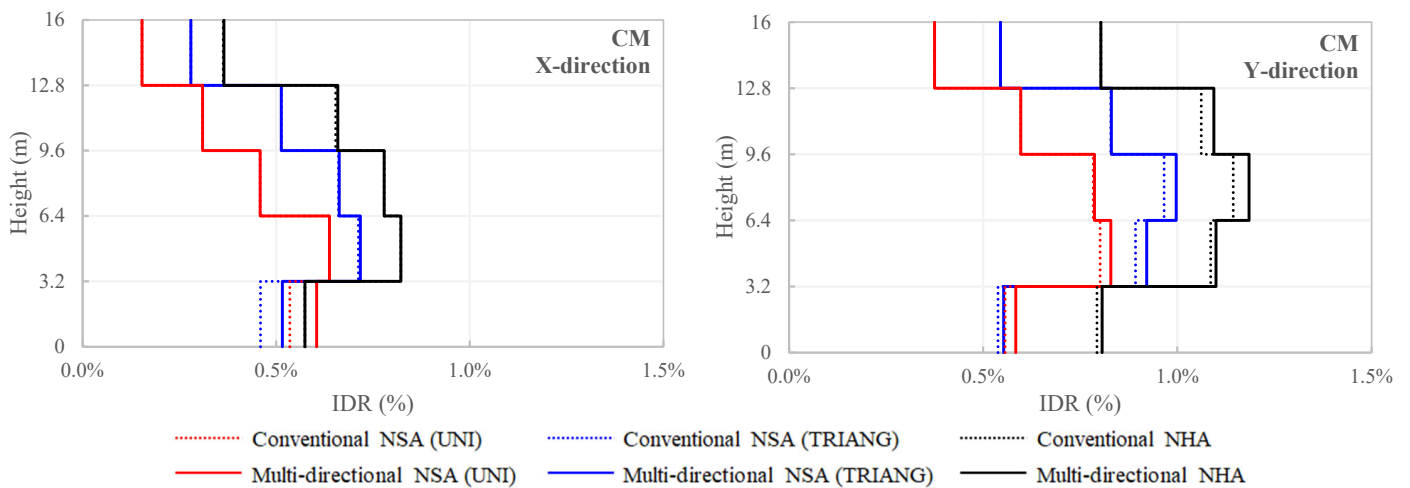


Figure 20. Structure 1 IDRs at CM for NSAs (red and blue lines) and NHAs (black lines) following a conventional load orientation (dotted lines) and a multi-directional approach (continuous lines).

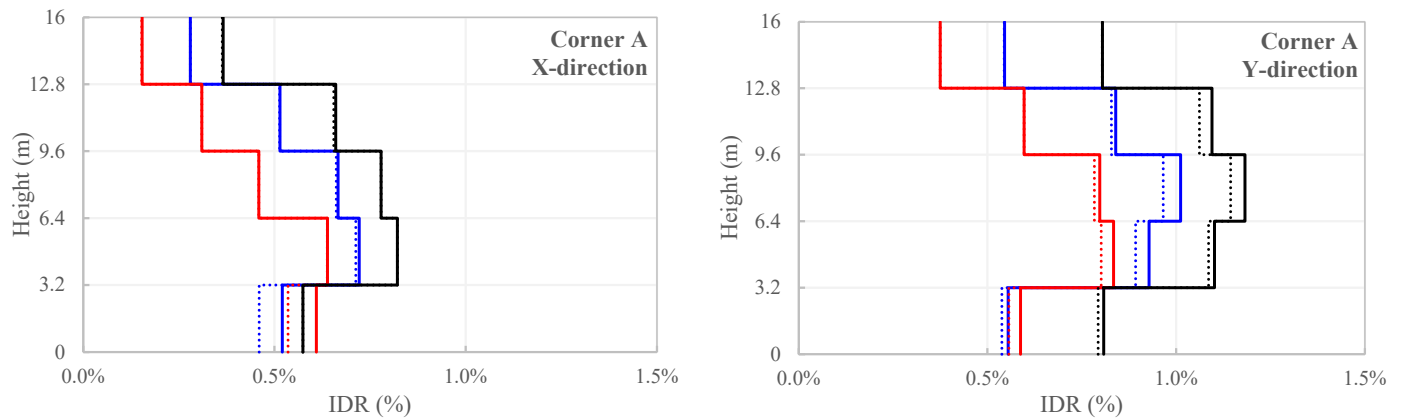


Figure 21. Structure 1 IDRs at Corner A.

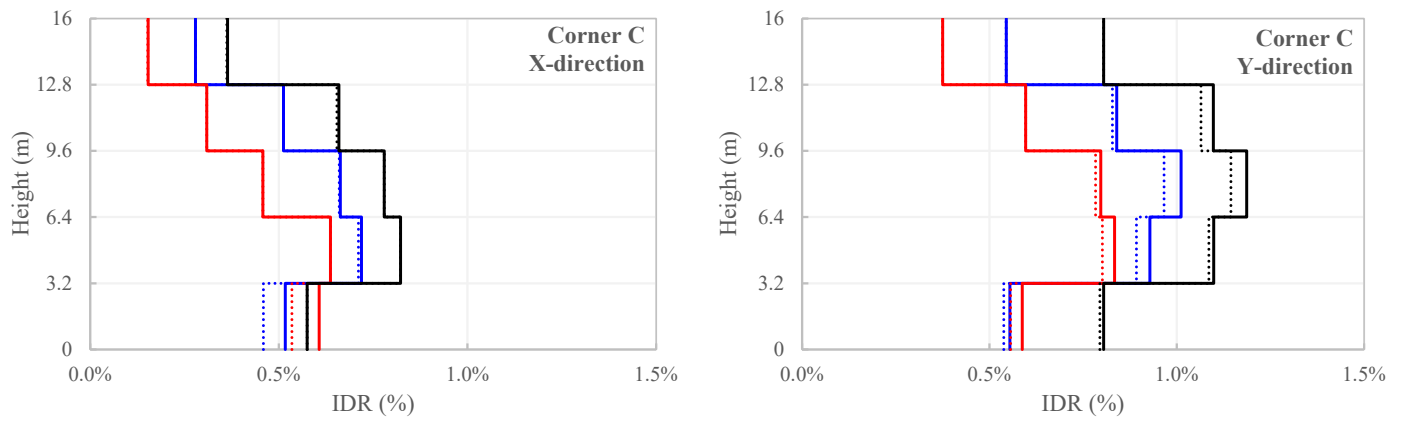
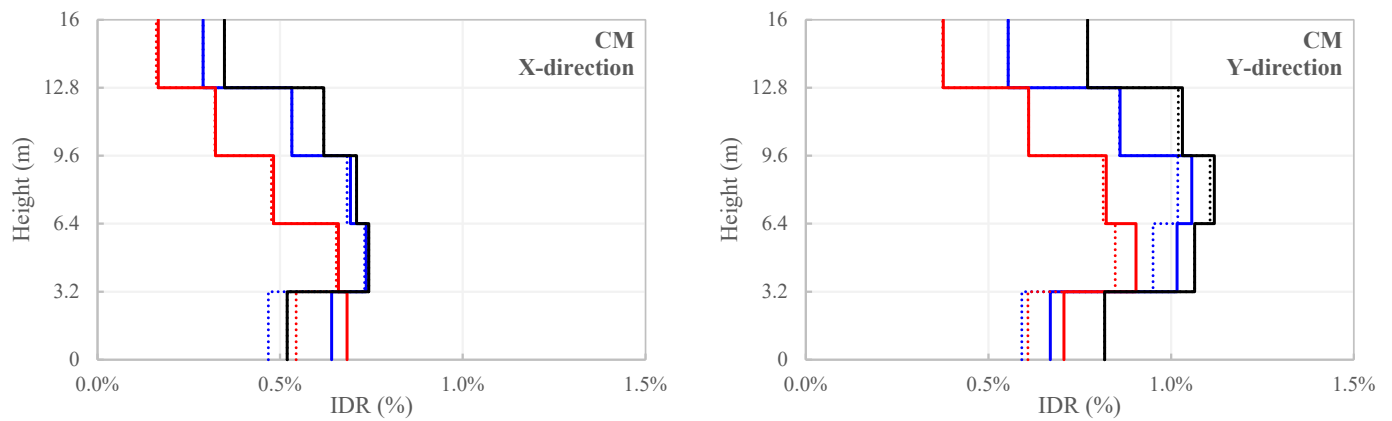


Figure 22. Structure 1 IDRs at Corner C.



..... Conventional NSA (UNI)
 Conventional NSA (TRIANG)
 Conventional NHA
——— Multi-directional NSA (UNI)
 ——— Multi-directional NSA (TRIANG)
 ——— Multi-directional NHA

Figure 23. Structure 2 IDRs at CM for NSAs (red and blue lines) and NHAs (black lines) following a conventional load orientation (dotted lines) and a multi-directional approach (continuous lines).

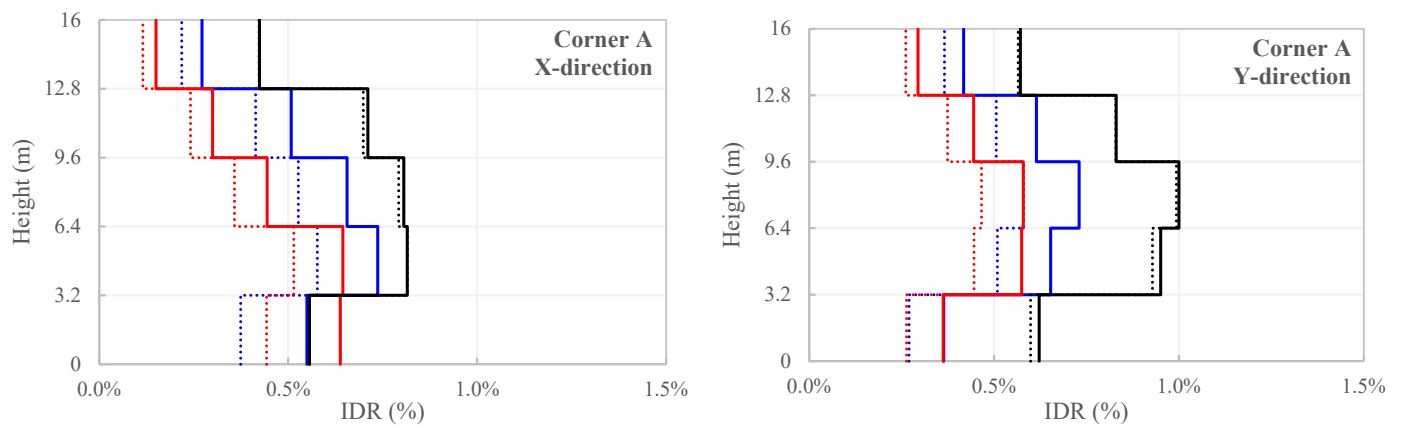


Figure 24. Structure 2 IDRs at Corner A.

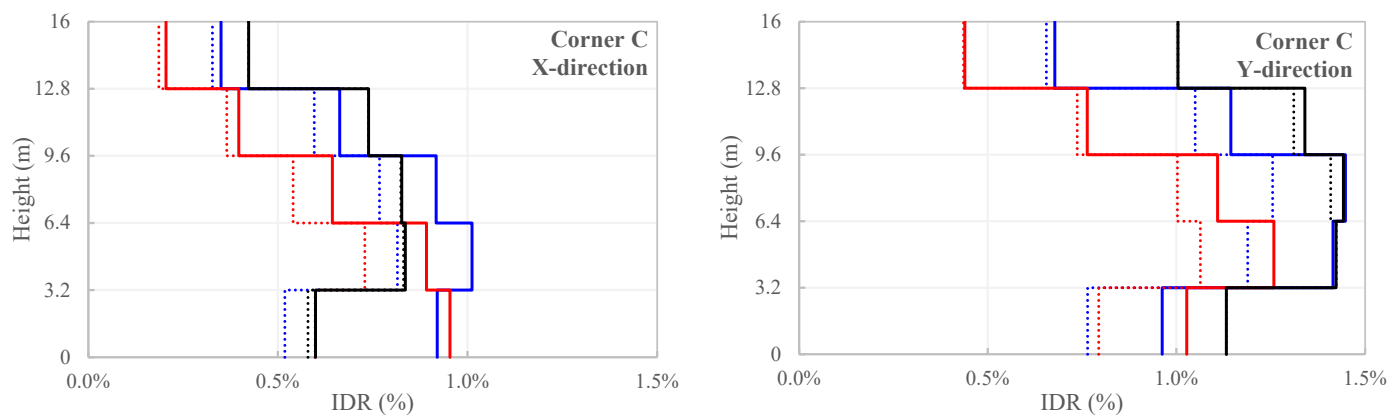


Figure 25. Structure 2 IDRs at Corner C.

The results for Str1 indicate that at CM (Figure 20), Corner A (Figure 21) and Corner C (Figure 22) the multi-directional NSAs predict demands regularly lower than those predicted by the multi-directional NHAs, especially at the upper floors and for mass proportional loading patterns. The triangular load pattern leads to IDRs closer to those of the NHAs. Moreover, the application of the seismic inputs along the conventional 0° , 90° , 180° and 270° directions provide demands that are lower than the corresponding ones for multidirectional inputs (both static and dynamic), but the differences are not significant. As previously stated, this result is due to the double symmetry of the structural configuration. Moreover, for the NHAs the use of a significant number of records makes the results of a multi-directional analyses similar to those obtained along the reference directions. This is a general result that is due to the fact that the different record pairs have different principal directions; thus, as the number of records increases, the multi-directionality of the input is included in the input ground records [24,30].

Figures 23–25 show the same results for Str2. For this structure: (a) the demands at CM for the multi-directional NSAs with triangular loads are very close to those for the multi-directional NHAs; (b) the demands at Corner A indicate that the multi-directional NHAs are more conservative than the multi-directional NSAs; (c) at Corner C the demands for the multi-directional NSAs with triangular loads are closer to those of the NHAs than for Corner A. At the lower levels, the multi-directional NSAs in the X direction are more conservative than the NHA, indicating a different failure mechanism (at the ground level for the NSAs, at the second and/or third floors for the other analyses).

The complete results of CM of Str2 for all nonlinear analyses are shown in the polar plots of Figures 26 and 27 for the X and Y directions, respectively. Each figure shows five polar graphs, one for each level. Each plot shows the IDRs of the multi-directional NHAs (in black) and of the multi-directional NSAs with mass proportional (UNI, in red) and triangular (TRIANG, in blue) load patterns. The grey dots represent the IDRs for the 20 selected ground motion records applied at a given angle θ , while the black line connects the points corresponding to the average values of the 20 maximum IDRs obtained for each direction. All plots show that the IDR_Y values are greater than the IDR_X values because of the larger structure flexibility in the Y direction. In the X direction (Figure 26), IDR_X for multi-directional NSAs with triangular load pattern are comparable with the corresponding results for NHAs, especially at the first three levels. In the Y direction (Figure 27), the differences between multi-directional NSAs and NHAs are greater than those in the X direction, especially at Levels 1, 4 and 5, where the NSAs can be significantly unconservative. It appears that, except for Level 1, the UNI (mass proportional) load pattern consistently underestimates the IDR demand. This result stresses the fact for multi-directional NSAs too it is important to consider at least two load patterns, where UNI leads to larger demands at the ground level and TRIANG leads to larger demands at the higher levels.

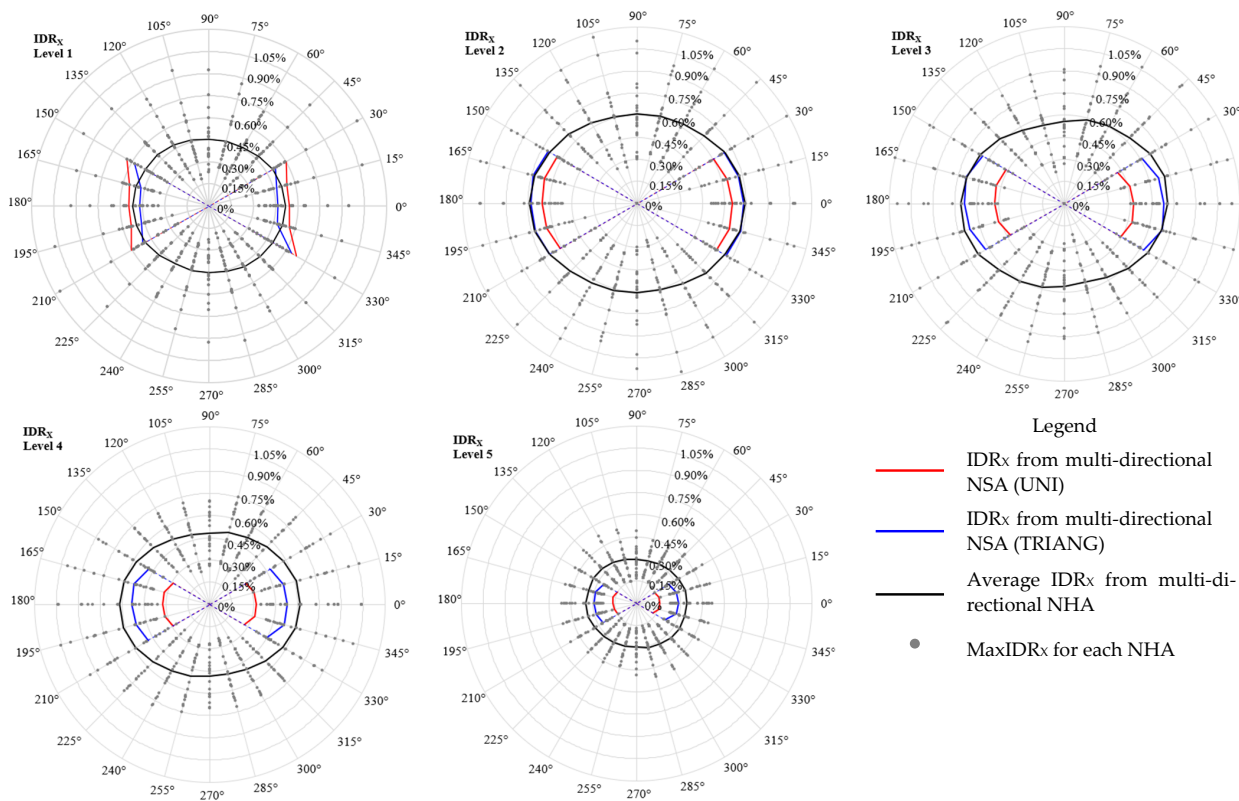


Figure 26. Structure 2: polar plots of IDR_x at CM for NHAs (black) and NSAs with mass proportional (in red) and triangular (in blue) load patterns.

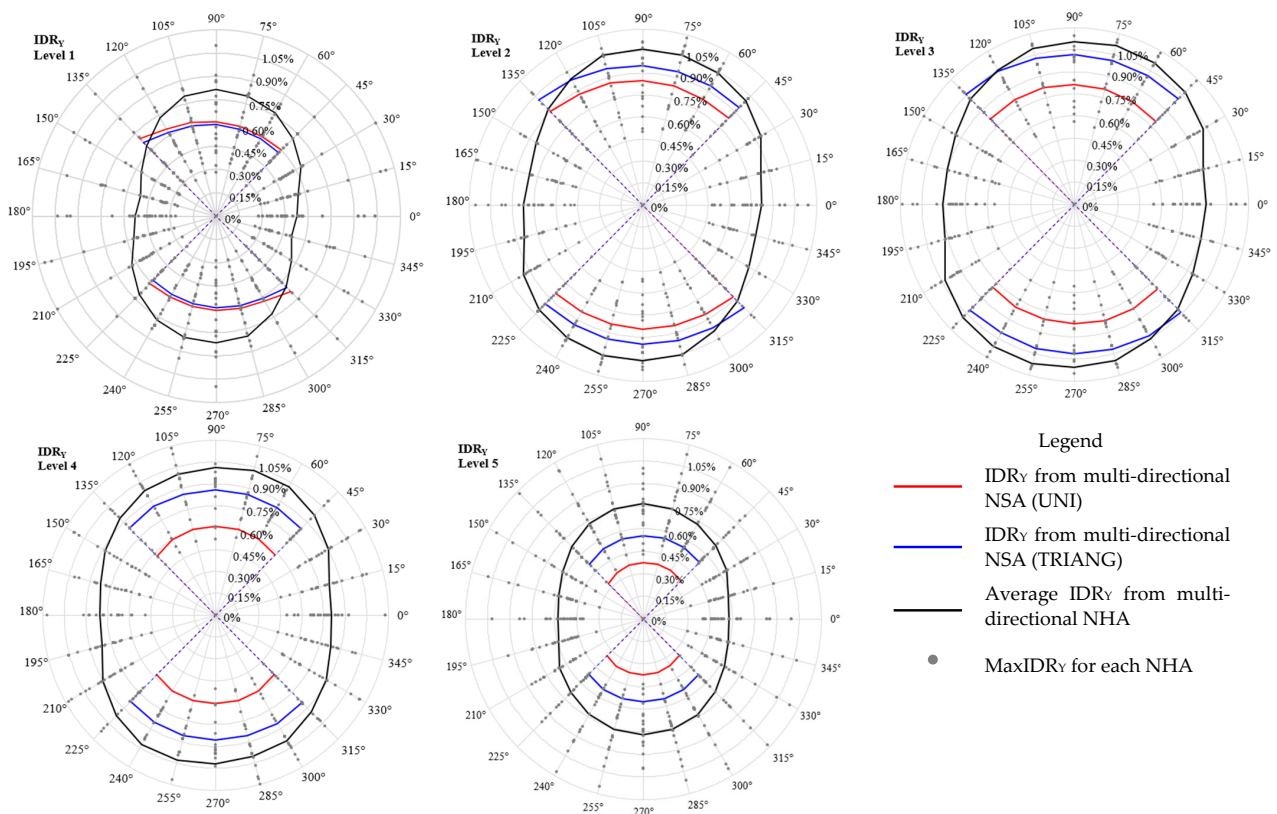


Figure 27. Structure 2: polar plots of IDR_y at CM for NHAs (black) and NSAs with mass proportional (in red) and triangular (in blue) load patterns.

5. Summary and Conclusions

Several studies show the importance of considering the directionality of the input forces in seismic analyses of existing structures. For NHAs, the problem is solved when a large set of ground motions is used. In this case there is no need to rotate the ground motion inputs. This paper confirms this result. For NSAs, often used in design practice and research to avoid the large computational cost of NHAs, the problem is not well studied. This paper analyses the variability in structural demands for multi-directional NSAs and compares the results with those of NHAs.

Two case-study structures representative of Italian RC buildings of the 1970s are considered. Structure 1 is roughly doubly symmetric, while Structure 2 has significant asymmetry caused by the translation of CM by about 15% of the building plan dimensions. In both structures, the load-bearing and perimetral frames have deep beams while the other frames have flat beams. The following multi-directional nonlinear static procedure is proposed in order to account for the directionality of the seismic input:

- Step 1: A set of PO analyses are sequentially carried out by applying mass proportional and triangular load patterns at 24 different incident angles θ with 15° increments;
- Step 2: For each θ , the V_b - θ PO curves are obtained in the X and Y directions for CM and two corners;
- Step 3: For each θ , the PO curve (of the two computed at Step 2) that reaches a peak and then softens (and thus is assumed to have reached failure) is selected as the reference PO curve. When both PO curves reach the peak and then soften, the PO curve with the maximum displacement is assumed as the reference PO;
- Step 4: For each load pattern and θ , the structural demand in terms of IDR is computed using the N2 method. The IDR is in the direction of the reference PO curve selected in Step 3.

The procedure applied in this research presents the following innovative points:

1. It clarifies the methodology that is applied to find the structural demand in multi-directional NSAs;
2. It indicates two load patterns (mass proportional and triangular) that can be used to carry out multi-directional NSA and easily compute the relevant participation factors;
3. It shows how the structural capacity and demand are affected by the interaction between the buildings' responses in the X and Y directions for loading angles different from 0° and 90° ;
4. It validates the proposed approach through multi-directional NSAs on two buildings (one plan regular, the other plan asymmetric obtained by changing the position of the center of mass). The NSA results are compared with those of multi-directional NHAs.

The multi-directional NSAs clearly show that at angles different from the building's X and Y directions the base shear capacity of the building along X and Y decreases due to the interaction between the X and Y responses. This behavior is captured thanks to the fiber section discretization of the columns that accounts for biaxial bending and axial load interaction.

The results of the multi-directional NSAs are compared with those of the multi-directional NHAs. For the NHAs a ground motion set of 20 pairs of spectrum-compatible ground motion records scaled to T_1 are selected. The 20 pairs are applied parallel to the same angles θ used in the NSAs. For a given θ , the maximum IDR in each direction for all 20 NHAs and their average values is computed.

The multi-directional NSAs on Structure 1 show results that are similar to those for the conventional NSAs (i.e., PO along the X and Y building directions). Conversely, the results of multi-directional NSAs on Structure 2 are significantly more conservative than those of conventional NSAs, especially at the building corners. For Structure 2, the ratio of the maximum IDR of multi-directional and conventional NSAs at Corner C for $\theta = 330^\circ$ is equal to 1.77.

The comparison of the IDRs from multi-directional NSAs and NHAs shows the following results: (a) application of the input records in the NHAs does not lead to significant changes, as already shown in previous studies; (b) in most cases, the multi-directional NSAs are unconservative with respect to the results of the NHAs; (c) however, the multi-directional NSAs improves the prediction with respect to the conventional NSAs and the improvement is more significant for the asymmetric Structure 2; (d) as expected, the mass proportional pattern leads to higher IDR demands at the ground level, while at the upper levels the triangular load pattern leads to higher demands; (e) For the asymmetric Structure 2, the demands predicted by the NSAs on the building corners tends to be rather unconservative with respect to the NHAs.

In conclusion, this paper proposed a new Nonlinear Static Analysis procedure to account for the multi-directionality of the seismic input. The results show that the demands can be significantly higher than those for conventional NSAs where the building is pushed in the X and Y building directions. These results are more evident for the asymmetric case study structure. However, the results from NHAs are in general more conservative than for NSAs, even when the multi-directionality is accounted for.

Author Contributions: Conceptualization, C.C.; methodology, C.C.; software, C.C., M.T. and G.C.; validation, C.C. and M.T.; formal analysis, C.C. and M.T.; investigation, C.C. and G.C.; data curation, C.C. and M.T.; writing—original draft preparation, C.C.; writing—review and editing, C.C. and E.S.; visualization, C.C.; supervision, E.S.; project administration, E.S.; funding acquisition, E.S. All authors have read and agreed to the published version of the manuscript.

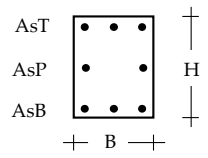
Funding: The study presented in this article was partially funded by the Italian Civil Protection Agency (DPC) through Project ReLUIS-DPC 2019–2021 (WP11). The opinions and conclusions presented by the authors do not necessarily reflect those of the funding agency.

Data Availability Statement: All relevant data are contained within the article.

Conflicts of Interest: The authors declare no conflict of interest.

Appendix A. Cross Sections and Reinforcements of the Columns of the Case-Study Buildings

Table A1. Size and reinforcement of the columns' cross sections.

COLUMNS										
Story	n.	1-8-25-32	2-7-26-31	3-6-27-30	4-5-28-29	9-16-17-24	10-15-18-23	11-14-19-22	12-13-20-21	
5	Size	30 × 50	30 × 50	30 × 50	30 × 50	30 × 50	30 × 50	30 × 50	30 × 50	AsT AsP AsB
	AsT	2φ14	2φ14	2φ14	2φ14	2φ14	2φ14	2φ14	2φ14	
	AsP	1φ14	1φ14	1φ14	1φ14	1φ14	1φ14	1φ14	1φ14	
	AsB	2φ14	2φ14	2φ14	2φ14	2φ14	2φ14	2φ14	2φ14	
4	Size	30 × 55	30 × 50	30 × 50	30 × 55	30 × 55	30 × 50	30 × 50	30 × 55	AsT AsP AsB
	AsT	2φ14	2φ14	2φ14	2φ14	2φ14	2φ14	2φ14	2φ14	
	AsP	1φ14	1φ14	1φ14	1φ14	1φ14	1φ14	1φ14	1φ14	
	AsB	2φ14	2φ14	2φ14	2φ14	2φ14	2φ14	2φ14	2φ14	
3	Size	30 × 55	30 × 55	30 × 55	30 × 55	30 × 55	30 × 55	30 × 55	30 × 55	AsT: top rebars AsP: intermediate rebars AsB: bottom rebars
	AsT	2φ14	2φ14	2φ14	2φ14	2φ14	2φ14	2φ14	2φ14	
	AsP	1φ14	1φ14	1φ14	1φ14	1φ14	1φ14	1φ14	1φ14	
	AsB	2φ14	2φ14	2φ14	2φ14	2φ14	2φ14	2φ14	2φ14	
2	Size	30 × 60	30 × 55	30 × 55	30 × 60	30 × 60	30 × 55	30 × 55	30 × 60	AsT AsP AsB
	AsT	2φ14	2φ14	2φ14	2φ14	2φ14	2φ14	2φ14	2φ14	
	AsP	1φ14	1φ14	1φ14	1φ14	1φ14	2φ14	2φ14	1φ14	
	AsB	2φ14	2φ14	2φ14	2φ14	2φ14	2φ14	2φ14	2φ14	
1	Size	30 × 60	30 × 60	30 × 60	30 × 60	30 × 60	30 × 60	30 × 60	30 × 60	AsT AsP AsB
	AsT	2φ14	2φ14	2φ14	2φ14	2φ14	3φ14	3φ14	2φ14	
	AsP	1φ14	1φ14	1φ14	1φ14	2φ14	2φ14	2φ14	2φ14	
	AsB	2φ14	2φ14	2φ14	2φ14	2φ14	3φ14	3φ14	2φ14	

Appendix B. Selected Ground Motion Records

Table A2. Seismological features of the 20 selected records.

n.	Database	Station ID	Earthquake Name	Date	Time (UTC)	Mw	Epicentral Distance (km)	Site Class	Scale Factor
1	ESD	ST20	Friuli	06/05/1976	20:00:13	6.5	23	A	1.2734
2	ESD	ST54	Tabas	16/09/1978	15:35:57	7.3	12	A	0.8692
3	ESD	ST98	Campano Lucano	23/11/1980	18:34:52	6.9	25	A	2.8740
4	ESD	ST161	Golbasi	05/05/1986	03:35:38	6	29	A	4.1699
5	ESD	ST2486	South Iceland	17/06/2000	15:40:41	6.5	5	A	0.4186
6	ESD	ST2487	South Iceland	17/06/2000	15:40:41	6.5	13	A	2.1493
7	ESD	ST2496	South Iceland (aftershock)	21/06/2000	00:51:48	6.4	14	A	1.3983
8	ESD	ST2486	South Iceland (aftershock)	21/06/2000	00:51:48	6.4	22	A	3.2431
9	ESD	ST2557	South Iceland (aftershock)	21/06/2000	00:51:48	6.4	15	A	1.6217
10	ESD	ST2563	South Iceland (aftershock)	21/06/2000	00:51:48	6.4	24	A	3.5147
11	ESD	ST2497	South Iceland (aftershock)	21/06/2000	00:51:48	6.4	20	A	2.1600
12	ESD	ST2558	South Iceland (aftershock)	21/06/2000	00:51:48	6.4	5	A	0.4782
13	ESD	ST539	Bingol	01/05/2003	00:27:04	6.3	14	A	1.0089
14	ESM	MZ19	Central Italy	30/10/2016	06:40:18	6.5	22.6	A	0.6537
15	ESM	ULA	Northwestern Balkan Peninsula	15/04/1979	06:19:41	6.9	19.7	A	0.7204
16	ESM	ATH4	Greece	07/09/1999	11:56:49	5.9	19.7	A	3.6782
17	ESM	CLO	Central Italy	26/10/2016	19:18:06	5.9	10.8	A	1.5432
18	ESM	CLO	Central Italy	30/10/2016	06:40:18	6.5	7.8	A	0.3685
19	ESM	MMO	Central Italy	26/10/2016	19:18:06	5.9	16.2	A	2.4060
20	ESM	T1213	Central Italy	30/10/2016	06:40:18	6.5	12	A	0.5742

References

1. *ENV 1998-1*; Eurocode 8-Part 1: Eurocode 8 Design Provisions for Earthquake Resistance of Structures. Part 1-1: General Rules—Seismic Actions and General Requirements for Structures. CEN: Brussels, Belgium, 2005.
2. *NTC2018*; Decreto Ministeriale 17/01/2008 (DM 14/01/2018). Norme Tecniche per le Costruzioni, Ministero delle Infrastrutture, GU n.29 04/02/2008: Rome, Italy, 2018.
3. *ASCE/SEI 7-16*; Minimum Design Loads and Associated Criteria for Buildings and Other Structures. ASCE Standard, American Society of Civil Engineers, Structural Engineering Institute: Reston, VA, USA, 2016.
4. *ASCE/SEI 41-17*; Seismic Evaluation and Retrofit of Existing Buildings. American Society of Civil Engineers: Reston, VA, USA, 2017.
5. Newmark, N.M.; Rosenblueth, E. *Fundamentals of Earthquake Engineering*; Prentice-Hall: Hoboken, NJ, USA, 1971.
6. Newmark, N.M. Seismic design criteria for structures and facilities, Trans-Alaska pipeline system. In Proceedings of the U.S. National Conference on Earthquake Engineering, Ann Arbor, MI, USA, 18–20 June 1975; Earthquake Engineering Institute Michigan: Ann Arbor, MI, USA, 1975; pp. 94–103.
7. Rosenblueth, E.; Contreras, H. Approximate design for multicomponent earthquakes. *J. Eng. Mech. Div.* **1977**, *103*, 881–893. [[CrossRef](#)]
8. Wilson, E.L.; Suharwardy, I.; Habibullah, A. A clarification of the orthogonal effects in a three-dimensional seismic analysis. *Earthq. Spectra* **1995**, *11*, 659–666. [[CrossRef](#)]
9. Menun, C.; Der Kiureghian, A. A replacement for the 30%, 40% and SRSS rules for multi-component seismic analysis. *Earthq. Spectra* **1998**, *14*, 153–156. [[CrossRef](#)]

10. López, O.A.; Chopra, A.K.; Hernández, J.J. Evaluation of combination rules for maximum response calculation in multicomponent seismic analysis. *Earthq. Eng. Struct. Dyn.* **2001**, *30*, 1379–1398. [[CrossRef](#)]
11. López, O.A.; Chopra, A.K.; Hernández, J.J. Adapting the CQC3 rule for three seismic components with different spectra. *J. Struct. Eng.* **2004**, *130*, 403–410. [[CrossRef](#)]
12. Wang, J.; Burton, H.V.; Dai, K. Combination rules used to account for orthogonal seismic effects: State-of-the-art review. *J. Struct. Eng.* **2019**, *145*, 03119001. [[CrossRef](#)]
13. Cimellaro, G.P.; Giovine, T.; Lopez-Garcia, D. Bidirectional pushover analysis of irregular structures. *J. Struct. Eng.* **2014**, *140*, 04014059. [[CrossRef](#)]
14. Fajfar, P. A nonlinear analysis method for performance-based seismic design. *Earthq. Spectra* **2000**, *16*, 573–592. [[CrossRef](#)]
15. Fajfar, P.; Marusic, D.; Perus, I. Torsional effects in the pushover-based seismic analysis of buildings. *J. Earthq. Eng.* **2005**, *9*, 831–854. [[CrossRef](#)]
16. Fernandez-Davila, I.; Cominetti, S.; Cruz, E.F. Considering the bi-directional effects and the seismic angle variations in building design. In Proceedings of the 12th World Conference on Earthquake Engineering, Auckland, New Zealand, 30 January–4 February 2000.
17. Athanatopoulou, A.M. Critical orientation of three correlated seismic components. *Eng. Struct.* **2005**, *27*, 301–312. [[CrossRef](#)]
18. Tsourekas, A.G.; Athanatopoulou, A.M. Evaluation of existing combination rules for the effects caused by three spatial components of an earthquake. *KSCE J. Civ. Eng.* **2013**, *17*, 1728–1739. [[CrossRef](#)]
19. Rigato, A.B.; Medina, R.A. Influence of angle of incidence on seismic demands for inelastic single-storey structures subjected to bi-directional ground motions. *Eng. Struct.* **2007**, *29*, 2593–2601. [[CrossRef](#)]
20. Kostinakis, K.G.; Athanatopoulou, A.M.; Avramidis, I.E. Evaluation of inelastic response of 3D singlestorey R/C frames under bi-directional excitation using different orientation schemes. *Bull. Earthq. Eng.* **2013**, *11*, 637–661. [[CrossRef](#)]
21. Morfidis, K.; Kostinakis, K.; Karakostas, C. Comparative evaluation of different damage measures for reinforced concrete building considering variable incident angles. In Proceedings of the 4th ECCOMAS Thematic Conference on Computational Methods in Structural Dynamics and Earthquake Engineering, Kos Island, Greece, 12–14 June 2013.
22. Vargas, Y.F.; Pujades, L.G.; Barbat, A.H.; Hurtado, J.E. Risk assessment of reinforced concrete buildings considering the earthquake directionality effects. In Proceedings of the 4th ECCOMAS Thematic Conference on Computational Methods in Structural Dynamics and Earthquake Engineering, Kos Island, Greece, 12–14 June 2013.
23. Magliulo, G.; Maddaloni, G.; Petrone, C. Influence of earthquake direction on the seismic response of irregular plan RC frame buildings. *Earthq. Eng. Eng. Vib.* **2014**, *13*, 243–256. [[CrossRef](#)]
24. Cantagallo, C.; Camata, G.; Spacone, E. Influence of ground motion selection methods on seismic directionality effects. *Earthq. Struct.* **2015**, *8*, 185–204. [[CrossRef](#)]
25. Kalkan, E.; Reyes, J.C. Significance of rotating ground motions on behavior of symmetric-and asymmetric-plan structures: Part II. Multi-story structures. *Earthq. Spectra* **2015**, *31*, 1613–1628. [[CrossRef](#)]
26. Reyes, J.C.; Kalkan, E. Significance of rotating ground motions on behavior of symmetric-and asymmetric-plan structures: Part I. Single-story structures. *Earthq. Spectra* **2015**, *31*, 1591–1612. [[CrossRef](#)]
27. Mitropoulou, C.C.; Lagaros, N.D. Critical incident angle for the minimum cost design of low, mid and high-rise steel and reinforced concrete-composite buildings. *Int. J. Optim. Civil. Eng.* **2016**, *6*, 135–158.
28. Giannopoulos, D.; Vamvatsikos, D. Ground motion records for seismic performance assessment: To rotate or not to rotate? *Earthq. Eng. Struct. Dyn.* **2018**, *47*, 2410–2425. [[CrossRef](#)]
29. Amarloo, N.; Emami, A.R. A 3-dimensional perspective for inter-storey drift, ductility and damage distributions in plan-irregular RC buildings considering seismic orientation effect. *Bull. Earthq. Eng.* **2019**, *17*, 3447–3474. [[CrossRef](#)]
30. Skoulidou, D.; Romão, X. The significance of considering multiple angles of seismic incidence for estimating engineering demand parameters. *Bull. Earthq. Eng.* **2020**, *18*, 139–163. [[CrossRef](#)]
31. Di Sarno, L.; Amiri, S.; Garakaninezhad, A. Effects of incident angles of earthquake sequences on seismic demands of structures. *Structures* **2020**, *28*, 1244–1251. [[CrossRef](#)]
32. Cannizzaro, F.; Pantò, B.; Lepidi, M.; Caddemi, S.; Caliò, I. Multi-directional seismic assessment of historical masonry buildings by means of macro-element modelling: Application to a building damaged during the L'Aquila earthquake (Italy). *Buildings* **2017**, *7*, 106. [[CrossRef](#)]
33. Chácara, C.; Cannizzaro, F.; Pantò, B.; Caliò, I.; Lourenço, P.B. Seismic vulnerability of URM structures based on a Discrete Macro-Element Modeling (DMEM) approach. *Eng. Struct.* **2019**, *201*, 109715. [[CrossRef](#)]
34. Kalkbrenner, P.; Pelà, L.; Sandoval, C. Multi directional pushover analysis of irregular masonry buildings without box behavior. *Eng. Struct.* **2019**, *201*, 109534. [[CrossRef](#)]
35. Ghayoumian, G.; Emami, A.R. A Multi-Direction Pushover Procedure for Seismic Response Assessment of Low-To-Medium-Rise Modern Reinforced Concrete Buildings with Special Dual System Having Torsional Irregularity. *Structures* **2020**, *28*, 1077–1107. [[CrossRef](#)]
36. Antoniou, S.; Pinho, R. Development and verification of a displacement-based adaptive pushover procedure. *J. Earthq. Eng.* **2004**, *8*, 643–661. [[CrossRef](#)]
37. Kalkan, E.; Kunnath, S.K. Assessment of current nonlinear static procedures for seismic evaluation of buildings. *Eng. Struct.* **2007**, *29*, 305–316. [[CrossRef](#)]

38. Bosco, M.; Ferrara, G.A.; Gherzi, A.; Marino, E.M.; Rossi, P.P. Predicting displacement demand of multi-storey asymmetric buildings by nonlinear static analysis and corrective eccentricities. *Eng. Struct.* **2015**, *99*, 373–387. [[CrossRef](#)]
39. Bosco, M.; Gherzi, A.; Marino, E.M.; Rossi, P.P. Generalized corrective eccentricities for nonlinear static analysis of buildings with framed or braced structure. *Bull. Earthq. Eng.* **2017**, *15*, 4887–4913. [[CrossRef](#)]
40. McKenna, F.; Scott, M.H.; Fenves, G.L. Nonlinear finite-element analysis software architecture using object composition. *J. Comput. Civ. Eng.* **2010**, *24*, 95–107. [[CrossRef](#)]
41. Petracca, M.; Candeloro, F.; Camata, G. *STKO User Manual*; ASDEA Software Technology: Pescara, Italy, 2017.
42. Scott, M.H.; Fenves, G.L. Plastic Hinge Integration Methods for Force-Based Beam-Column Elements. *J. Struct. Eng.* **2006**, *132*, 244–252. [[CrossRef](#)]
43. *ACI CODE-318-19*; Building Code Requirements for Structural Concrete and Commentary, 2022. American Concrete Institute: Farmington Hills, MI, USA, 2022.
44. *Circolare 21 gennaio 2019, n. 7 C.S.LL.PP.*; Istruzioni per l'Applicazione dell'«Aggiornamento delle “Norme Tecniche Per le Costruzioni”» di cui al DM 17 Gennaio 2018. Ministero delle Infrastrutture e dei Trasporti: Rome, Italy, 2019. (In Italian)
45. Spacone, E.; Filippou, F.C.; Taucer, F.F. Fibre beam-column model for non-linear analysis of R/C frames: Part I. Formulation. *Earthq. Eng. Struct. Dyn.* **1996**, *25*, 711–725. [[CrossRef](#)]
46. Kent, D.C.; Park, R. Flexural members with confined concrete. *J. Struct. Div. ASCE* **1971**, *97*, ST7. [[CrossRef](#)]
47. Terrenzi, M.; Spacone, E.; Camata, G. Comparison between Phenomenological and Fiber- Section Non-linear Models. *Front. Built. Environ.* **2020**, *6*, 38. [[CrossRef](#)]
48. Lima, C.; Angiolilli, M.; Barbagallo, F.; Belletti, B.; Bergami, A.V.; Camata, G.; Cantagallo, C.; Di Domenico, M.; Fiorentino, G.; Gherzi, A.; et al. Nonlinear Modeling Approaches for Existing Reinforced Concrete Buildings: The Case Study of De Gasperi-Battaglia School Building in Norcia. In *Lecture Notes in Civil Engineering*; Springer: Cham, Switzerland, 2020; Volume 42. [[CrossRef](#)]
49. Barbagallo, F.; Bosco, M.; Marino, E.M.; Rossi, P.P. On the fibre modelling of beams in RC framed buildings with rigid diaphragm. *Bull. Earthq. Eng.* **2020**, *18*, 189–210. [[CrossRef](#)]
50. *Decreto ministeriale del 30/05/1974*; Norme Tecniche per la Esecuzione delle Opere in Cemento Armato Normale e Precompresso e per le Strutture Metalliche, Ministero dei Lavori Pubblici, Gazzetta Ufficiale Serie Generale n. 198 del 29/07/1974. Ministero dei Lavori Pubblici: Rome, Italy, 1974.
51. Bazzurro, P.; Allin Cornell, A.C. Disaggregation of seismic hazard. *Bull. Seismol. Soc. Am.* **1999**, *89*, 501–520. [[CrossRef](#)]
52. Barani, S.; Spallarossa, D.; Bazzurro, P. Disaggregation of probabilistic ground-motion hazard in Italy. *Bull. Seismol. Soc. Am.* **2009**, *99*, 2638–2661. [[CrossRef](#)]
53. Ambraseys, N.; Smit, P.; Douglas, G.; Margaris, B.; Sigbjornsson, R.; Ólafsson, S.; Suhadolc, P.; Costa, G. Internet-Site for European Strong-Motion Data, European Commission. *Boll. Geofis. Teor. Ed Appl.* **2004**, *45*, 113–129.
54. Luzi, L.; Puglia, R.; Russo, E. ORFEUS WG5. Engineering Strong Motion Database, version 1.0. In *Observatories & Research Facilities for European Seismology*; Istituto Nazionale di Geofisica e Vulcanologia: Rome, Italy, 2016. [[CrossRef](#)]
55. Beyer, K.; Bommer, J.J. Relationships between median values and between aleatory variabilities for different definitions of the horizontal component of motion. *Bull. Seismol. Soc. Am.* **2006**, *96*, 1512–1522. [[CrossRef](#)]
56. Kreslin, M.; Fajfar, P. The extended N2 method considering higher mode effects in both plan and elevation. *Bull. Earthq. Eng.* **2012**, *10*, 695–715. [[CrossRef](#)]
57. Fajfar, P.; Gašperšič, P. The N2 method for the seismic damage analysis of RC buildings. *Earthq. Eng. Struct. Dyn.* **1996**, *25*, 31–46. [[CrossRef](#)]
58. Cantagallo, C.; Camata, G.; Spacone, E. A Probability-Based Approach for the Definition of the Expected Seismic Damage Evaluated with Non-linear Time-History Analyses. *J. Earthq. Eng.* **2019**, *23*, 261–283. [[CrossRef](#)]

Disclaimer/Publisher's Note: The statements, opinions and data contained in all publications are solely those of the individual author(s) and contributor(s) and not of MDPI and/or the editor(s). MDPI and/or the editor(s) disclaim responsibility for any injury to people or property resulting from any ideas, methods, instructions or products referred to in the content.